

Quarterly Technical Report

Solid State Research

1987:2

Lincoln Laboratory
MASSACHUSETTS INSTITUTE OF TECHNOLOGY
LEXINGTON, MASSACHUSETTS



Prepared under Electronic Systems Division Contract F19628-85-C-0002.

Approved for public release; distribution unlimited.

ADA188388

The work reported in this document was performed at Lincoln Laboratory, a center for research operated by Massachusetts Institute of Technology, with the support of the Department of the Air Force under Contract F19628-85-C-0002.

This report may be reproduced to satisfy needs of U.S. Government agencies.

The views and conclusions contained in this document are those of the contractor and should not be interpreted as necessarily representing the official policies, either expressed or implied, of the United States Government.

The ESD Public Affairs Office has reviewed this report, and it is releasable to the National Technical Information Service, where it will be available to the general public, including foreign nationals.

This technical report has been reviewed and is approved for publication.

FOR THE COMMANDER



Thomas J. Alpert, Major, USAF
Chief, ESD Lincoln Laboratory Project Office

Non-Lincoln Recipients

PLEASE DO NOT RETURN

Permission is given to destroy this document
when it is no longer needed.

MASSACHUSETTS INSTITUTE OF TECHNOLOGY
LINCOLN LABORATORY

SOLID STATE RESEARCH

QUARTERLY TECHNICAL REPORT

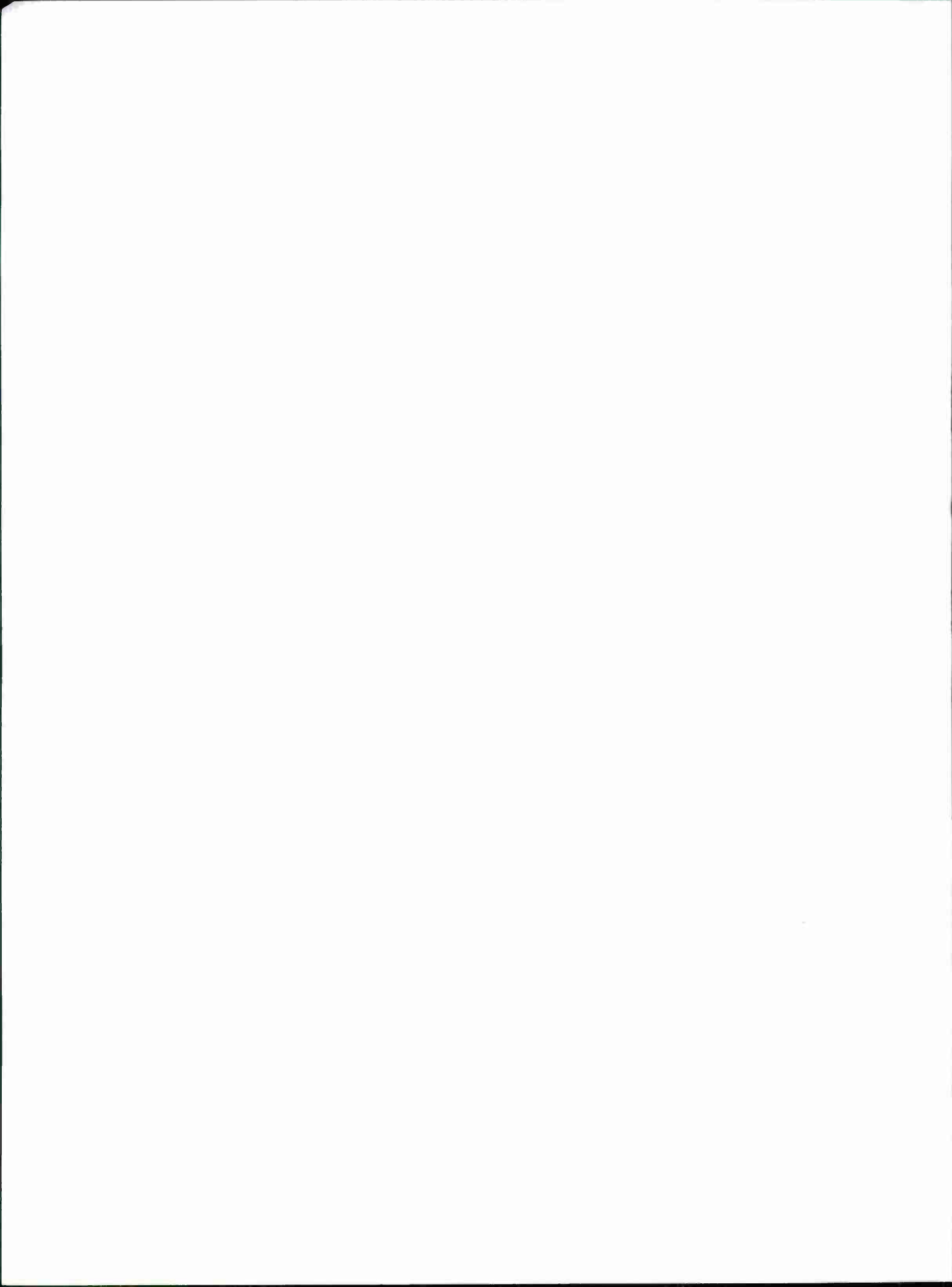
1 FEBRUARY — 30 APRIL 1987

ISSUED 21 AUGUST 1987

Approved for public release; distribution unlimited.

LEXINGTON

MASSACHUSETTS



ABSTRACT

This report covers in detail the solid state research work of the Solid State Division at Lincoln Laboratory for the period 1 February through 30 April 1987. The topics covered are Solid State Device Research, Quantum Electronics, Materials Research, Microelectronics, and Analog Device Technology. Funding is provided primarily by the Air Force, with additional support provided by the Army, DARPA, Navy, SDIO, NASA, and DOE.

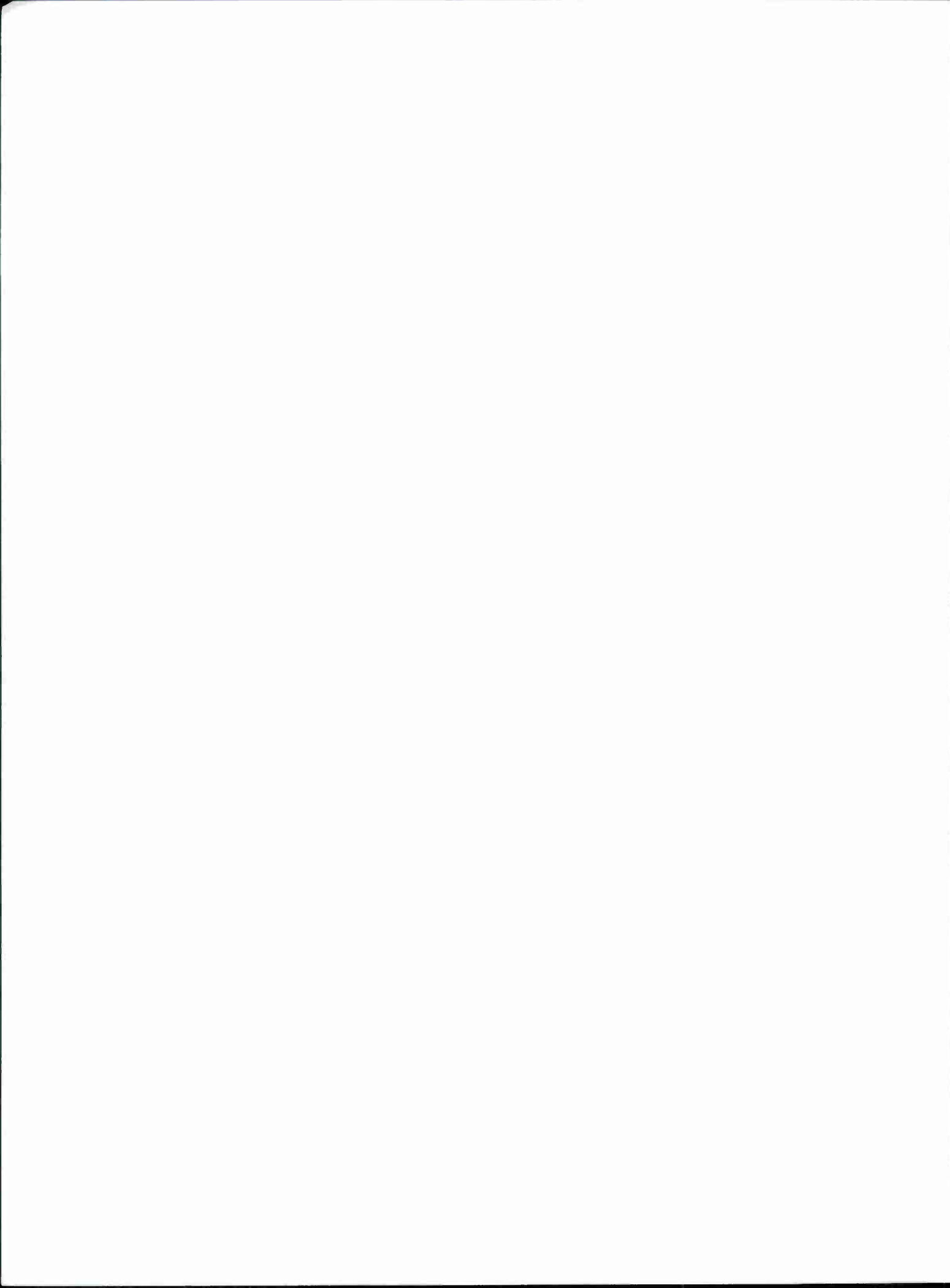
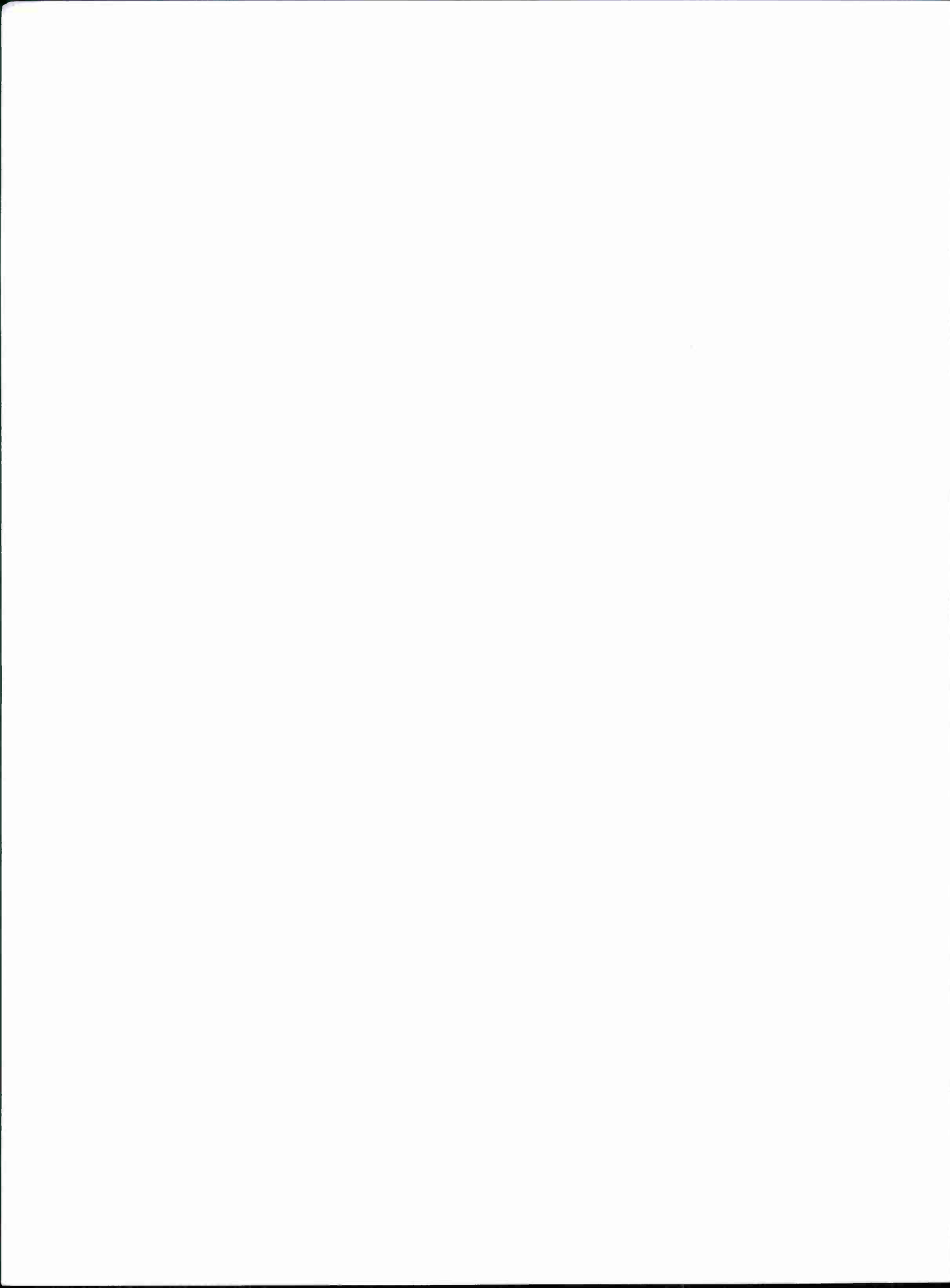


TABLE OF CONTENTS

Abstract	iii
List of Illustrations	vii
Introduction	xi
Reports on Solid State Research	xiii
Organization	xxiii
1. SOLID STATE DEVICE RESEARCH	1
1.1 Analysis of Junction Depths and Lattice Point Defect Interdiffusion Coefficients in $Hg_{0.8}Cd_{0.2}Te$	1
1.2 Capless Rapid Thermal Annealing of Si^+ -Implanted InP	5
1.3 Measurement of Intermodulation Distortion in Interferometric Modulators	7
2. QUANTUM ELECTRONICS	15
2.1 Stable Single-Frequency Ti: Al_2O_3 Ring Laser	15
2.2 Nd:YAG Sum-Frequency Generation of Sodium Resonance Radiation	18
2.3 Nonlinear Optical Effects in Semiconductor Coupled Quantum Wells	21
3. MATERIALS RESEARCH	25
3.1 Microwave MESFETs Fabricated in GaAs Layers Grown on Silicon-on-Sapphire Substrates	25
3.2 Optical Absorption and Photoluminescence of Ti: $ScBO_3$	29
4. MICROELECTRONICS	33
4.1 CCD Spatial Light Modulators Using InGaAs/GaAs Multiple Quantum Wells	33
4.2 Simulations of Si PBT	35
4.3 A New Method for Finding the Energy Spectra of Quantum-Well Structures	38
5. ANALOG DEVICE TECHNOLOGY	43
5.1 High-Transition-Temperature Oxide Superconductors	43
5.2 Integrated Circuit Implementation of an Artificial Neural Network Based on CCD and MNOS Technologies	45

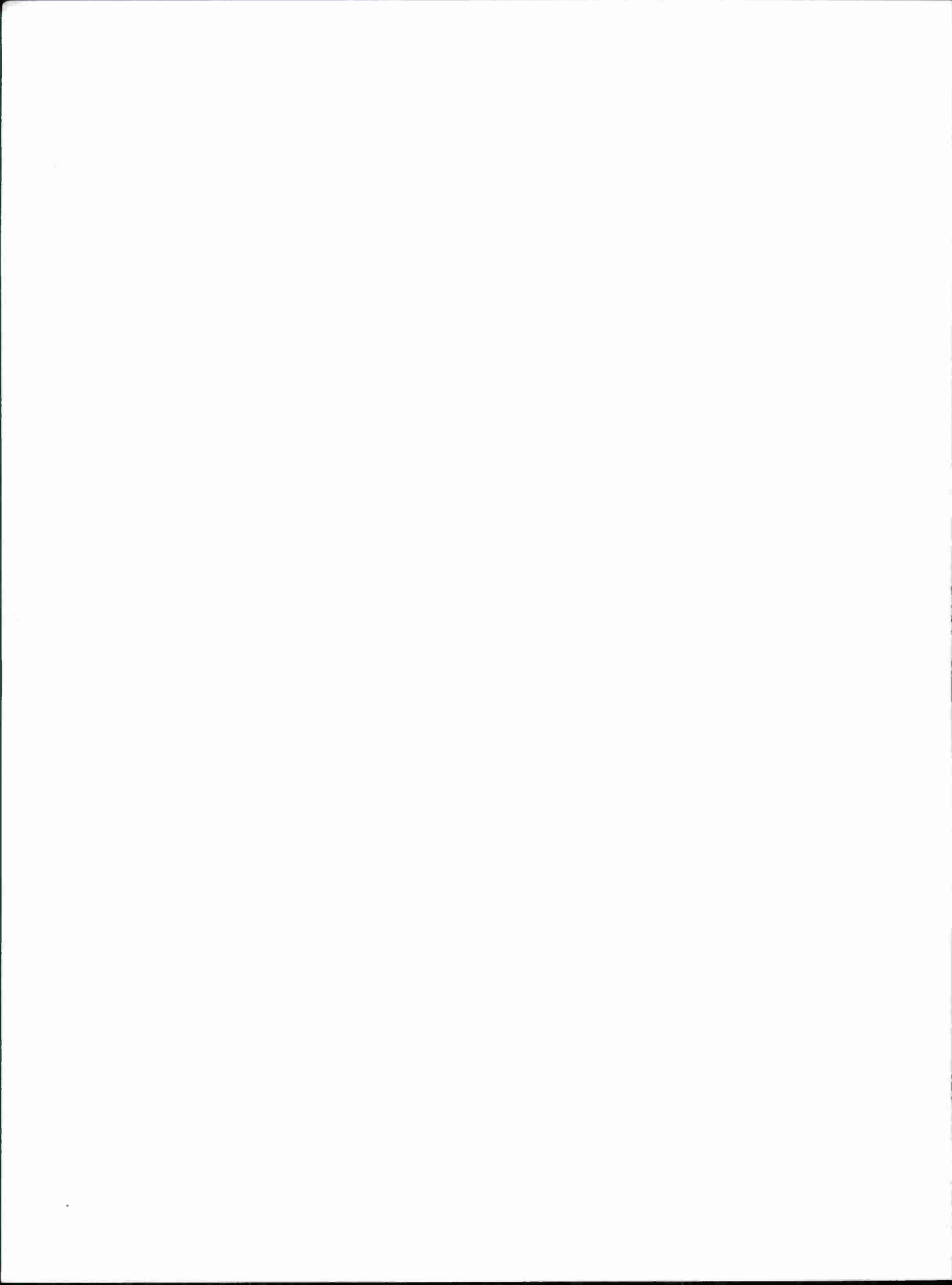


LIST OF ILLUSTRATIONS

Figure No.		Page
1-1	Schematic of Model Showing Hg Interstitial, Hg Vacancy, n-p Junction, and Part of a Te Precipitate	2
1-2	Ratio of n-p Junction Depth Squared x_j^2 to Diffusion Time t vs Temperature	3
1-3	Ratio of Diffusion Time to n-p Junction Depth Squared vs Excess Te Concentration	4
1-4	Extrinsic Carrier Concentration vs Isothermal Annealing Temperature for $\text{Hg}_{0.8}\text{Cd}_{0.2}\text{Te}$	4
1-5	Schematic Diagram of Sample Fixture Used for EOP Annealing Technique	6
1-6	Photomicrograph of Heat-Treated InP Surfaces: (a) EOP Anneal at 900°C for 10 s; (b) Conventional Anneal Using PSG Encapsulant at 750°C for 5 min	7
1-7	(a) Sheet Carrier Concentration and (b) Sheet Electron Mobility vs Anneal Temperature for InP Samples Implanted with 140-keV 10^{14}-cm^{-2} Si^+ Which Were Annealed Using EOP and Conventional Techniques for Several Anneal Times. Legend in (a) is Applicable to (b).	8
1-8	Analog Optical-Fiber Communication Link Consisting of Constant-Power Optical Source, Interferometric Modulator, Optical Fiber, Detector, and Amplifier	9
1-9	Photograph of Spectrum Analyzer Trace of Amplified Photodetector Output for Case Where $V_I/V_\pi = 0.16$. Both Fundamental and Dominant Intermodulation Signals Can Be Seen.	10
1-10	Plot of Fundamental and Intermodulation Product Power Levels as a Function of Electrical Drive Power. Solid Lines Are Theoretical Predictions, with Extrapolations to Intermodulation Intercept Shown Dashed; Crosses Are Experimental Results.	11
2-1	Single-Frequency Power vs Wavelength. Output Power of 100 mW Can Be Obtained Over 100-nm Wavelength Range with a Maximum Output Power of 200 mW. Dip in Middle Is Caused by Laser Cavity Optics.	15
2-2	Frequency Changes in 5 min. A Least-Squares Linear Fit of Frequency Is Indicated.	16

Figure No.		Page
2-3	Ti:Al ₂ O ₃ Laser Threshold vs Ar-Ion Pump Laser Power for Four Different Positions of Ti:Al ₂ O ₃ Crystal	17
2-4	Tuning Curves of 1.064- and 1.319- μ m Continuous Nd:YAG Lasers	18
2-5	Spectral Lineshapes of Two Continuous Nd:YAG Lasers and Corresponding Sum-Frequency Radiation Generated in a Nonlinear Crystal	19
2-6	Upper and Middle Traces Show Shapes of 1.064- and 1.319- μ m Q-Switched Nd:YAG Lasers, Respectively. Lower Trace Shows Pulse Shape of Sum-Frequency Radiation.	20
2-7	Schemes for Light-By-Light Modulation. Signal Beam Can Propagate Either (a) Parallel or (b) Normal to CQW Plane. Interaction Occurs in CQW Layers. Excitonic Dipole Moments Are Also Symbolically Shown.	22
2-8	Evidence of Change of CQW Dipole Moments Induced by Pump Light. At High Intensity, Excitonic Line Labeled (e ₁ , h ₁) Blue Shifts, Which Is Consistent with a Reduction in Strength of Internal Electric Field.	22
2-9	Time-Resolved Study of Exciton Blue Shift Shown in Figure 2-8. Modulation of a Weak Signal Beam by an Intense Pump Beam Is Measured as a Function of Delay Between Two Pulses. (a) For Pump Excitation Above Exciton Absorption Line, Carriers Are Generated, Creating Dipole Screening Which Lasts for Carrier Lifetime. (b) For Excitation Below Exciton Transition, a Faster Effect Is Observed and Interpreted as a Result of Virtual Screening. Time Resolution of Measurement Is 10 ps.	23
3-1	Schematic Diagram of MGSOS Microwave MESFET	26
3-2	Gate Schottky Diode Characteristic of MGSOS Microwave MESFET	27
3-3	Transistor Characteristics of MGSOS Microwave MESFET with Transconductance of \sim 140 mS/mm	27
3-4	MSG, MAG, and Current Gain vs Frequency for MGSOS Microwave MESFET with $f_{\max} = 20$ GHz and $f_T \simeq 8$ GHz	28
3-5	Transmission Spectrum of a Cleaved Single-Crystal Sample of Ti:ScBO ₃ at Room Temperature. Maximum Transmission of 40 Percent Was Limited by Fresnel Losses and Surface Scattering.	30

Figure No.		Page
3-6	Absorption Spectra at Room Temperature for Ti:ScBO ₃ and Ti:Al ₂ O ₃	30
3-7	Photoluminescence Intensity vs Time for Ti:ScBO ₃ at 80 K	31
4-1	Cross Section of a CCD SLM Using an InGaAs/GaAs MQW Structure	33
4-2	Electrical Performance of a 16-Stage CCD SLM at a 1-MHz Data Rate. Upper Trace Shows 16 Sampling Pulses Applied to an Input Gate and Lower Trace Is CCD Output.	34
4-3	Three Impurity Profiles Used in Simulations of Si PBT: (1) Uniformly As-Doped Epilayer; (2) 400 keV, 3.2×10^{12} -cm ⁻² P Implant; and (3) 300 keV, 2.8×10^{12} -cm ⁻² P Implant	36
4-4	Simulated Collector I-V Characteristics for Devices with Profiles 1 and 3	36
4-5	Simulated Collector I-V Characteristics for Devices with Profiles 2 and 3	37
4-6	A Comparison of Experimental Collector I-V Characteristics and Those Obtained by CANDE for a 400-keV Implanted Device	38
4-7	Electron Potential Energy Diagram of a Resonant-Tunneling Heterostructure with 0.7-V Bias Applied. Structure Consists of a Pair of Double-Barrier Structures Separated by 500 Å Undoped GaAs. Each Double-Barrier Structure Has Two 15-Å-Wide AlAs Regions Separated by a 45-Å-Wide GaAs QW. Three Dashed Energy Levels (Drawn to Scale) Correspond to Three Peaks in Transmission Probability Curve Shown in Figure 4-8.	40
4-8	Transmission Probability vs Longitudinal Kinetic Energy for an Electron Incident on Structure Shown in Figure 4-7. A Voltage Drop of 0.7 V Is Assumed to Exist Across Structure.	40
5-1	Dc Resistance as a Function of Temperature for Bulk La _{1.85} Sr _{0.15} CuO ₄	43
5-2	Dc Resistance as a Function of Temperature for Bulk YBa ₂ Cu ₃ O ₇	44
5-3	N × N Hopfield Associative Memory	45
5-4	Single Synaptic Element Showing Fully Balanced Structure	46
5-5	Prototype MNOS/CCD Artificial Neural-Network Integrated Circuit	48
5-6	Experimental vs Theoretical Associative-Recall Performance of Artificial Neural Network	49



INTRODUCTION

1. SOLID STATE DEVICE RESEARCH

A model for the interdiffusion of lattice defects in $Hg_{0.8}Cd_{0.2}Te$ has been used to derive an equation for the junction depth obtained when a Te-rich sample is diffused under Hg-saturation conditions at low temperatures. Calculations using the equation are found to agree with experimental data for junction depth vs excess Te concentration, diffusion time, and temperature.

An enhanced-overpressure capless technique suitable for annealing ion-implanted InP at temperatures of 900°C has been developed that utilizes a Sn coating to provide a high local partial pressure of P. InP samples implanted with 140-keV 10^{14}-cm^{-2} Si^+ and annealed at 900°C for 10 s exhibited better electrical characteristics than samples annealed at 750°C for 5 min using conventional encapsulation techniques.

Two-tone intermodulation distortion in interferometric optical waveguide modulators has been measured. The experimental results closely follow the theoretical predictions.

2. QUANTUM ELECTRONICS

Single-frequency operation of a $Ti:Al_2O_3$ ring laser with an output power of 100 mW has been obtained over an 80-nm wavelength range. A frequency jitter of 15 MHz caused by argon ion laser power fluctuations limits the short-term stability; long-term frequency drift is caused by temperature variations in the laser enclosure. Thermal lensing compensation has been engineered into the laser to allow for high-power operation.

Radiation at the sodium D_2 resonance line has been generated with 8-percent efficiency by sum-frequency mixing the output radiation of two simultaneously Q-switched Nd:YAG lasers, one operating at $1.064\text{ }\mu m$ and the other at $1.319\text{ }\mu m$. By measuring the tuning curve of each Nd:YAG laser, it was found that the resonance radiation could be generated by operating the lasers at or near the peak of their gain curves.

Optical nonlinearities in coupled quantum well structures have been explored. The optical Kerr effect was observed and interpreted as the result of optically induced changes in the dipole strength of the coupled quantum well transition.

3. MATERIALS RESEARCH

Device-quality GaAs layers have been grown on silicon-on-sapphire substrates by molecular beam epitaxy. Microwave MESFETs (gate length of $0.8\text{ }\mu m$) with $g_m = 140\text{ mS/mm}$, $f_{max} = 20\text{ GHz}$, and $f_T = 8\text{ GHz}$ have been fabricated in these layers.

Optical absorption and photoluminescence due to Ti^{3+} ions have been measured for $Ti:ScBO_3$ crystals grown by the thermal gradient-freeze technique. The peak absorption occurs at 570 nm, compared with 490 nm in $Ti:Al_2O_3$. The luminescence lifetime is about $0.1\text{ }\mu s$ at 300 K and increases to about $1\text{ }\mu s$ at 77 K.

4. MICROELECTRONICS

A monolithic CCD-addressed spatial light modulator (SLM) using electroabsorption effects in InGaAs/GaAs multiple quantum wells has been successfully demonstrated. A contrast ratio of 1.33 has been observed at 965 nm in a 16-stage CCD SLM.

The I-V characteristics of ion-implanted Si PBT devices with different impurity profiles have been calculated by numerically solving the coupled, two-dimensional Poisson and current-continuity equations. Good agreement between experimental devices and the simulated results has been obtained.

A new technique has been developed to calculate the resonant tunneling transmission spectra and bound state energies in quantum-well heterostructures. The technique is superior to the standard transfer-matrix method in that it is much less susceptible to floating-point magnitude errors in relatively large structures and it can be executed about twice as fast.

5. ANALOG DEVICE TECHNOLOGY

High-transition-temperature oxide superconductors have been prepared in bulk form using ceramic processing techniques. Superconducting transition temperatures of 38 K for $\text{La}_{1.85}\text{Sr}_{0.15}\text{CuO}_4$ and 93 K for $\text{YBa}_2\text{Cu}_3\text{O}_7$ were achieved. Thin films have also been prepared; an onset of superconductivity was observed at 95 K in $\text{YBa}_2\text{Cu}_3\text{O}_7$ films.

A silicon integrated circuit which implements a dense array of synaptic coupling elements for an analog, programmable, nonvolatile artificial neural network has been designed and fabricated using CCD and metal-nitride-oxide-semiconductor technologies. The performance of this circuit has been studied by operating it in a Hopfield iterative-feedback network.

REPORTS ON SOLID STATE RESEARCH

1 February through 30 April 1987

PUBLISHED REPORTS

Journal Articles

JA No.

5871	Symmetric Three-Guide Optical Coupler with Non-identical Center and Outside Guides	J.P. Donnelly H.A. Haus* N. Whitaker	IEEE J. Quantum Electron. QE-23, 401 (1987)
5880	Prevention of Current Leakage in Mass-Transported GaInAsP/InP Buried-Heterostructure Lasers with Narrow Transported Regions	Z.L. Liau J.N. Walpole	IEEE J. Quantum Electron. QE-23, 313 (1987)
5883	Electron-Beam Programming and Testing of Complementary Metal-Oxide Semiconductor Systems	T.M. Lyszczarz S. Oliver J. Fried*	J. Vac. Sci. Technol. B 5, 97 (1987) DTIC AD-A178929
5885	Masked Ion Beam Lithography for Submicrometer-Gate-Length Transistors	S.W. Pang T.M. Lyszczarz C.L. Chen J.P. Donnelly J.N. Randall*	J. Vac. Sci. Technol. B 5, 215 (1987)
5891	Attainment of 0.13- μ m Lines and Spaces by Excimer-Laser Projection Lithography in "Diamond-Like" Carbon-Resist	M. Rothschild D.J. Ehrlich	J. Vac. Sci. Technol. B 5, 389 (1987), DTIC AD-A178914
5897	Hot-Jet Etching of Pb, GaAs, and Si	M.W. Geis N.N. Efremow S.W. Pang A.C. Anderson	J. Vac. Sci. Technol. B 5, 363 (1987), DTIC AD-A178905
5900	Visible-Laser Photochemical Etching of Cr, Mo, and W	M. Rothschild J.H.C. Sedlacek J.G. Black D.J. Ehrlich	J. Vac. Sci. Technol. B 5, 414 (1987)

* Author not at Lincoln Laboratory.

JA No.

5919	Millimeter-Band Oscillations Based on Resonant Tunneling in a Double-Barrier Diode at Room Temperature	E.R. Brown T.C.L.G. Sollner W.D. Goodhue C.D. Parker	Appl. Phys. Lett. 50 , 83 (1987)
5920	Sinusoidal and Digital High-Speed Modulation of p-Type Substrate Mass-Transported Diode Lasers	D.Z. Tsang Z.L. Liau	J. Lightwave Technol. LT-5 , 300 (1987)
5925	Radiation-Hardened Silicon-on-Insulator Junction Field-Effect Transistors Fabricated by a Self-Aligned Process	H.K. Choi B-Y. Tsaur C.K. Chen	IEEE Electron Device Lett. EDL-8 , 101 (1987)
5927	Observation of Millimeter-Wave Oscillations from Resonant Tunneling Diodes and Some Theoretical Considerations of Ultimate Frequency Limits	T.C.L.G. Sollner E.R. Brown W.D. Goodhue H.Q. Le	Appl. Phys. Lett. 50 , 332 (1987), DTIC AD-A178910
5930	High Accuracy Tuning of Planar Millimeter-Wave Circuits by Laser Photochemical Etching	D.J. Ehrlich D.F. Williams* J.H.C. Sedlacek M. Rothschild S.E. Schwarz*	IEEE Electron Device Lett. EDL-8 , 110 (1987)
5951	Large Monolithic Two-Dimensional Arrays of GaInAsP/InP Surface-Emitting Lasers	Z.L. Liau J.N. Walpole	Appl. Phys. Lett. 50 , 528 (1987)

Meeting Speeches**MS No.**

7039A	Lithium Niobate Serrodyne Frequency Translator for Fiber-Optic Gyroscopes	L.M. Johnson C.H. Cox, III	<i>Fiber Optic Gyros: 10th Anniversary Conference</i> , E. Udd, Ed., Proc. SPIE 719 , 141-145 (1987)
7049A	Growth and Characterization of Ti:Al ₂ O ₃ Crystals for Laser Applications	A.J. Strauss R.E. Fahey A. Sanchez R.L. Aggarwal	<i>Laser and Nonlinear Optical Materials</i> , L.G. DeShazer, Ed., Proc. SPIE 681 , 62-69 (1987)

* Author not at Lincoln Laboratory.

MS No.

7104A	Room Temperature cw Operation of a Ti:Al ₂ O ₃ Laser	A. Sanchez R.E. Fahey A.J. Strauss R.L. Aggarwal	<i>Springer Series in Optical Sciences</i> , Vol. 52, edited by A.B. Budgor, L. Esterowitz, and L.G. DeShazer (Springer-Verlag, New York, 1987)
7123	Bulk-Acoustic-Wave Reflection-Grating Devices in Fe:LiNbO ₃	D.E. Oates J.Y. Pan	Proc. Sixth IEEE International Symposium on Applications of Ferroelectrics, Bethlehem, Pennsylvania, 8-11 June 1986, pp. 66-71, DTIC AD-A178931
7124C	Small-Signal Modulation of p-Substrate Mass-Transported GaInAsP/InP Lasers	D.Z. Tsang Z.L. Liau	<i>Progress in Semiconductor Laser Diodes</i> , E. Eichen, Ed., Proc. SPIE 723, 50-54 (1986)
7155	Cermet as an Inorganic Resist for Ion Lithography	J. Melngailis D.J. Ehrlich S.W. Pang J.N. Randall	J. Vac. Sci. Technol. B 5, 379 (1987)
7203	A Technology for Optical Interconnections Based on Multichip Integration	D.Z. Tsang D.L. Smythe A. Chu* J.J. Lambert*	Opt. Eng. 25, 1127 (1986), DTIC AD-A174852; also in <i>Integration and Packaging of Optoelectronic Devices</i> , D.H. Hartman, R.L. Holman, and D.P. Skinner, Eds., Proc. SPIE 703, 122-127 (1986)
7207	Monolithic Integration of Si and GaAs Devices	H.K. Choi G.W. Turner T.H. Windhorn B-Y. Tsaur	<i>Integration and Packaging of Optoelectronic Devices</i> , D.H. Hartman, R.L. Holman, and D.P. Skinner, Eds., Proc. SPIE 703, 156-163 (1986)
7223	On-Wafer Testing of GaInAsP/InP Mass-Transported Lasers	J.N. Walpole Z.L. Liau	<i>Progress in Semiconductor Laser Diodes</i> , E. Eichen, Ed., Proc. SPIE 723, 100-102 (1986)
7274	Adaptive and Matched Filtering with a SAW/FET Programmable Transversal Filter	J.B. Green D.E. Oates P.M. Grant D.L. Smythe	1986 Ultrasonics Symposium Proceedings (IEEE, New York, 1986), pp. 127-141

* Author not at Lincoln Laboratory.

MS No.

7275 Bulk Wave Reflection-
Grating Devices

D.E. Oates

1986 *Ultrasonics Symposium
Proceedings* (IEEE, New York,
1986), pp. 327-337

* * * * *

UNPUBLISHED REPORTS**Journal Articles****JA No.**

5928 Diode Lasers with Cylindrical Mirror Facets and Reduced Beam Divergence

J.N. Walpole
Z.L. Liau
L.J. Missaggia
D. Yap

Accepted by Appl. Phys. Lett.

5933 Analysis of Junction Depths and Lattice Point Defect Interdiffusion Coefficients in $Hg_{0.8}Cd_{0.2}Te$

T.C. Harman

Accepted by J. Vac. Sci.
Technol.

5936 Serrodyne Optical Frequency Translation with High Sideband Suppression

L.M. Johnson
C.H. Cox, III

Accepted by J. Lightwave
Technol.

5950 Stark Effect in $Al_xGa_{1-x}As$ /
GaAs Coupled Quantum Wells

H.Q. Le
J.J. Zaykowski
W.D. Goodhue

Accepted by Appl. Phys. Lett.

5968 Zone-Melting-Recrystallization Silicon-on-Insulator Technology

B-Y. Tsaur

Accepted by IEEE Circ.
Devices Mag.

Meeting Speeches***MS No.**

6713D Recent Developments in the Methods and Applications of Reactive Laser-Direct-Patterning Techniques

D.J. Ehrlich

NSF Workshop, San Diego,
California, 23 February 1987

* Titles of Meeting Speeches are listed for information only. No copies are available for distribution.

MS No.

6723B	<i>In Situ</i> Processing of Semiconductor Surfaces	D.J. Ehrlich	American Physical Society Meeting, New York, NY, 16-17 March 1987
7096B	Spectral Linewidth of Semiconductor Lasers	J. Harrison A. Mooradian	
7329A	Quantum Well Resonators	T.C.L.G. Sollner	
7004A	Millimeter-Wave Monolithic Circuits for Receivers and Transmitter Applications	C.L. Chen	Lincoln Laboratory Technical Seminar Series, MIT, 18 February 1987
7049B	Growth of Laser-Quality Ti:Al ₂ O ₃ Crystals by a Seeded Gradient-Freeze Technique	R.E. Fahey A.J. Strauss A. Sanchez R.L. Aggarwal	1987 Gordon Research Conference on Crystal Growth, Santa Barbara, California, 23-27 February 1987
7094A	A Comparison of Neural Network and Matched Filter Processing for Detecting Lines in Images	P.M. Grant J.P. Sage	Applied Physics Seminar, Royal Signals & Radar Establishment, Malvern, United Kingdom, 14 April 1987
7095D	An Artificial Neural Network Integrated Circuit Based on MNOS/CCD Principles	J.P. Sage K.E. Thompson R.S. Withers	IEEE Workshop on Neural Devices and Applications, Pasadena, California, 18-19 February 1987
7095E	Artificial Neural Network Implementations Using Charge-Coupled Device and MNOS Nonvolatile Analog Memory Technologies	J.P. Sage K.E. Thompson R.S. Withers	IEEE Workshop on Neural Networks and Neurocomputing, Raleigh, North Carolina, 3 April 1987
7227D	The Fabrication and Performance of the Permeable Base Transistor	C.O. Bozler	Seminar, Raytheon Co., Lexington, Massachusetts, 25 March 1987
7238B	Optics for Computation	P.L. Kelley	1986/1987 Fall and Spring Seminars, Itek, Lexington, Massachusetts, 19 February 1987
7269B, C	Etching with Directed Beams of Ions and Radicals	M.W. Geis N.N. Efremow G.A. Lincoln S.W. Pang	Seminar, IBM, Burlington, Vermont, 24 February 1987; American Vacuum Society, Cleveland, Ohio, 25 February 1987

MS No.

7351	A 100 ns 16-Point Discrete Cosine Transform Process	A.M. Chiang P.C. Bennett B.B. Kosicki R.W. Mountain G.A. Lincoln J.H. Reinold	ISSCC-87, Harriman, New York, 25-27 February 1987
7419	High Speed Circuit Technology	A.M. Chiang	
7352	Advances in the Technology for the Permeable Base Transistor	M.A. Hollis K.B. Nichols R.A. Murphy C.O. Bozler	Advanced Processing of Semiconductor Devices, Bay Point, Florida, 23-27 March 1987
7365	Diode Lasers with Cylindrical Mirror Facets and Reduced Beam Divergence	J.N. Walpole Z.L. Liau L.J. Missaggia D. Yap	Southwest Optics '87 Conference, Albuquerque, New Mexico, 9-13 February 1987
7394	Fabrication and Characterization of InP Fresnel Microlenses	V. Diadiuk J.N. Walpole Z.L. Liau	
7410	Large Monolithic Two-Dimensional Arrays of GaInAsP/InP Surface-Emitting Lasers	Z.L. Liau J.N. Walpole	CLEO '87, Baltimore, Maryland, 27 April — 1 May 1987
7390	Multistable Pulsation of InGaAsP Semiconductor Lasers with a Proton-Bombarded Segment	M. Kuznetsov* D.Z. Tsang J.N. Walpole Z.L. Liau E.P. Ippen*	
7402	Single Frequency Ti:Al ₂ O ₃ Ring Laser	P.A. Schulz A. Sanchez R.E. Fahey A.J. Strauss	CLEO '87, Baltimore, Maryland, 27 April — 1 May 1987
7404	Optical Absorption and Photoluminescence of Ti:ScBO ₃	R.L. Aggarwal A. Sanchez R.E. Fahey M.M. Stuppi A.J. Strauss	

* Author not at Lincoln Laboratory.

MS No.

7406	Electro-optic Tuning of a Ti:Al ₂ O ₃ Laser	V. Daneu A. Sanchez	CLEO '87, Baltimore, Maryland, 27 April — 1 May 1987
7407	Nd:YAG Frequency Generation of Sodium Resonance Radiation	T.H. Jeys D.K. Killinger J. Harrison A. Mooradian	
7408	Second Harmonic Generation Using a Long Pulse Nd:YAG Laser	K. Wall N. Menyuk W.E. DeFeo	
7416	Phonon-Assisted Upconversion in 1.64 μ m Er:YAG Lasers	D.K. Killinger	
7434	Thoughts on the Junction Laser — the Past: 1962-1987, and the Future: 1987-2012	R.H. Rediker	
7391	Laser Photochemical Etching of Molybdenum and Tungsten Thin Films by Surface Halogenation	M. Rothschild J.H.C. Sedlacek D.J. Ehrlich	Second Topical Meeting on Microphysics of Surfaces, Beams, and Adsorbates, Sante Fe, New Mexico, 16-18 February 1987
7395	<i>In Situ</i> Excimer Laser Irradiation of GaAs Surfaces During Schottky Barrier Formation	P.A. Maki D.J. Ehrlich	
7412	Angled Etching Techniques for the Fabrication of Sub-50-nm-Wide GaAs Structures	W.D. Goodhue S.W. Pang G.D. Johnson D.K. Astolfi D.J. Ehrlich	1987 IEEE Workshop on Micrometer and Submicrometer Lithography, Marcos Island, Florida, 6-10 April 1987
7414	Laser-Based Microfabrication Technologies	D.J. Ehrlich	
7415	Point Contact Transistors and Schottky Diodes Formed on Synthetic Boron-Doped Diamonds	M.W. Geis D.D. Rathman D.J. Ehrlich R.A. Murphy	1987 Spring Meeting of the Materials Research Society, Anaheim, California, 21-25 April 1987
7426	Prospects for Monolithic GaAs/Si Integration	H.K. Choi G.W. Turner B-Y. Tsaur	

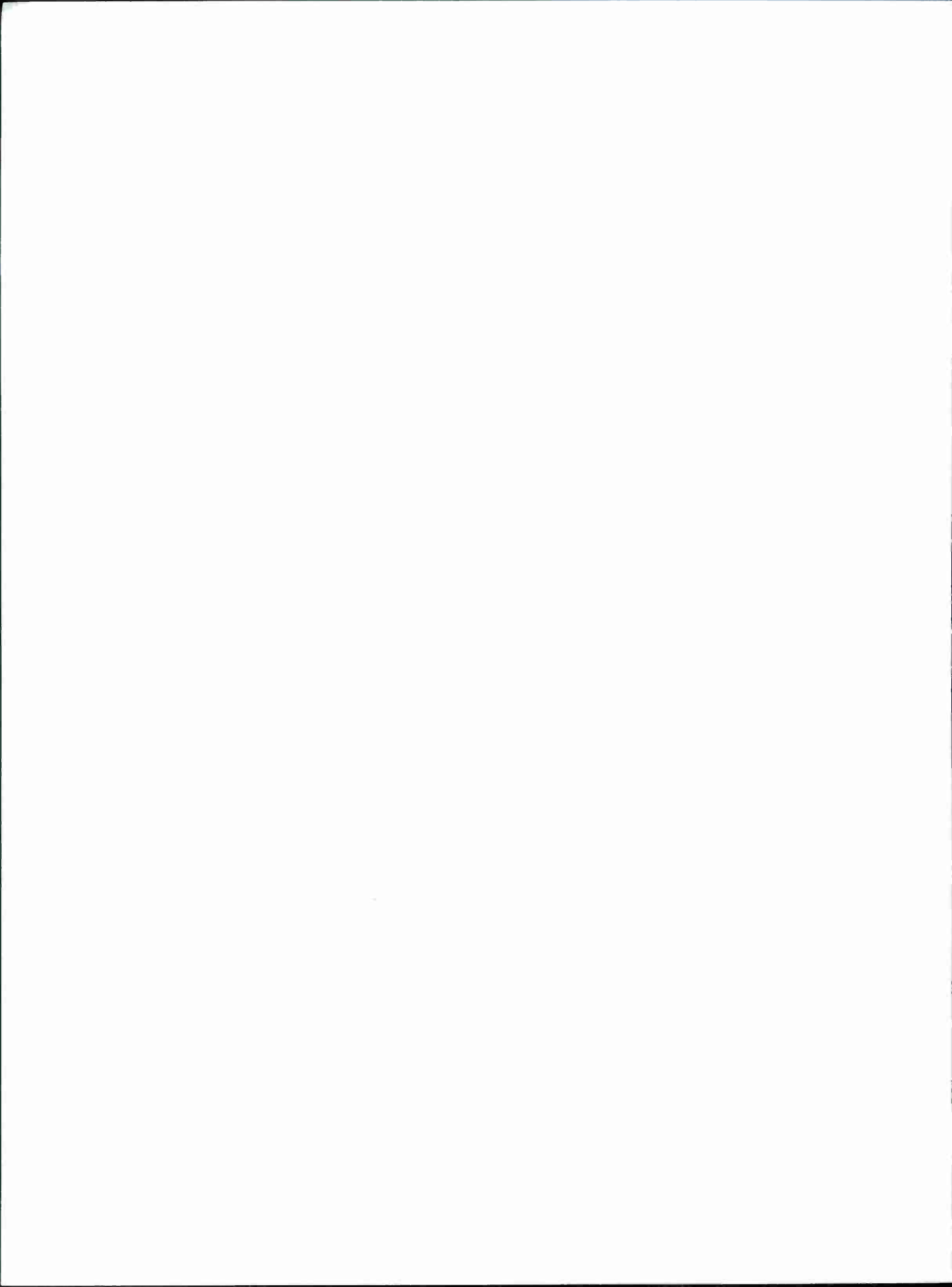
MS No.

7418	Stark Effect in $Al_xGa_{1-x}As/GaAs$ Coupled Quantum Wells	H.Q. Le J.J. Zayhowski W.D. Goodhue	IQEC '87, Baltimore, Maryland, 27 April — 1 May 1987
7451A	Ti:Al ₂ O ₃ Tunable Solid State Laser Technology	A. Sanchez	Symposium, Columbia Radiation Laboratory Series on Pure and Applied Science, Columbia University, New York, 1 April 1987
7460	Nearly Ballistic Resonant Tunneling	T.C.L.G. Sollner E.R. Brown W.D. Goodhue H.Q. Le C.L. Chen	Workshop on Ballistic Electrons for Transistors, Santa Barbara, California, 22-26 March 1987
7532	Micrometer Vacuum Tubes	M.W. Geis M. Rothschild D.J. Ehrlich	
7461	Recent Advances in Analog Signal Processing	P.M. Grant R.S. Withers	Applied Physics Seminar, Royal Signals & Radar Establishment, Malvern, United Kingdom, 13 April 1987
7498, 7498A	High Temperature Point Contact Transistors and Schottky Diodes Formed on Synthetic Boron-Doped Diamond	M.W. Geis	Seminar, Nano-Technology Group, MIT, 19 February 1987; Seminar, IBM, Yorktown, Heights, New York, 4 March 1987
7502	Receiver Technology for the Millimeter and Sub-millimeter-Wave Regions	B.J. Clifton	IEEE MTT Section Meeting, Long Island, New York, 25 February 1987
7514	Materials Issues for InP Bulk Crystal Technology	G.W. Iseler	WOCSEMMAD 1987, Hilton Head Island, South Carolina, 1-5 March 1987
7516	Production Applications of Laser Microchemistry	D.C. Shaver* N.P. Economou* L.A. Stern* D.J. Ehrlich	SPIE Symposium on Lasers in Microlithography, Santa Clara, California, 5 March 1987

* Author not at Lincoln Laboratory.

MS No.

7529	Resonant-Tunneling Oscillators	E.R. Brown T.C.L.G. Sollner W.D. Goodhue	Submillimeter Receiver Con- ference, Lake Arrowhead, California, 7-8 April 1987
7543	Silicon Integrated Circuit Implementation of an Arti- ficial Neural Network Based on MNOS and CCD Technologies	K.E. Thompson J.P. Sage R.S. Withers	Meeting on Neural Networks for Computing, Snowbird, Utah, 1 April 1987
7548	High- T_c Oxide Supercon- ductors — Requirements for Wideband Analog Devices	M.S. Dilorio	New England Regional Con- ference on High-Temperature Superconductivity, Boston University, 16 April 1987
7550	Superconducting Signal Processing Technology	R.W. Ralston	Superconductivity Symposium, Arlington, Virginia, 30 April 1987



ORGANIZATION

SOLID STATE DIVISION

A.L. McWhorter, *Head*
I. Melngailis, *Associate Head*
E. Stern, *Associate Head*
J.F. Goodwin, *Assistant*

N.L. DeMeo, Jr., *Associate Staff*

QUANTUM ELECTRONICS

A. Mooradian, *Leader*
P.L. Kelley, *Associate Leader*

Aggarwal, R.L.	McClung, S.
Barch, W.E.	Menyuk, N.
Belanger, L.J.	Sanchez-Rubio, A.
Brailove, A.A.	Seppala, J.P.
Daneu, V.	Schulz, P.A.
DeFeo, W.E.	Sharpe, K.A.
Hancock, R.C.	Sullivan, D.J.
Hryniwicz, J.V.	Tapper, R.
Jeys, T.H.	Tong, F.F.-K.*
Killinger, D.K.	Wall, K.F.
Lacovara, P.	Walker, W.A.
Le, H.Q.	Zayhowski, J.J.

ELECTRONIC MATERIALS

A.J. Strauss, *Leader*
B-Y. Tsaur, *Assistant Leader*
H.J. Zeiger, *Senior Staff*

Anderson, C.H., Jr.
Button, M.J.
Chen, C.K.
Choi, H.K.
Connors, M.K.
Delaney, E.J.
Eglash, S.J.
Fahey, R.E.
Finn, M.C.
Iseler, G.W.
Kolesar, D.F.
Krohn, L., Jr.
Mastromattei, E.L.
Mattia, J.P.
Nitishin, P.M.
Pantano, J.V.
Tracy, D.M.
Turner, G.W.
Wang, C.A.
Young, K.K.

APPLIED PHYSICS

R.C. Williamson, *Leader*
D.L. Spears, *Assistant Leader*
T.C. Harman, *Senior Staff*
R.H. Rediker, *Senior Staff*

Aull, B.F.	Groves, S.H.
Betts, G.E.	Hovey, D.L.
Bossi, D.E.*	Johnson, L.M.
Chan, S.K.*	Ketteridge, P.A.
Corcoran, C.J.*	Liau, Z.L.
Cox, C.H., III	Lind, T.A.
Diadiuk, V.	Metze, G.M.
Donnelly, J.P.	Molter, L.A.*
Ferrante, G.A.	O'Donnell, F.J.

Palmacci, S.T.
Palmateer, S.C.
Plonko, M.C.
Reeder, R.E.
Tsang, D.Z.
Walpole, J.N.
Woodhouse, J.D.
Yap, D.*
Yee, A.C.

* Research Assistant

ANALOG DEVICE TECHNOLOGY

R.W. Ralston, *Leader*
R.S. Withers, *Associate Leader*

Anderson, A.C.	Frickey, J.M.	Munroe, S.C.
Arsenault, D.R.	Green, J.B.	Oates, D.E.
Boisvert, R.R.	Holtham, J.H.	Pan, J.Y.*
Brogan, W.T.	Koulman, W.A.	Sage, J.P.
Denneno, A.P.	Lattes, A.L.	Slattery, R.L.
Dilorio, M.S.	Lichtenwalner, D.J.*	Thompson, K.E.†
Dolat, V.S.	Macedo, E.M., Jr.	Wong, S.C.*
Fitch, G.L.		

MICROELECTRONICS

W.T. Lindley, *Leader*
R.A. Murphy, *Associate Leader*
D.J. Ehrlich, *Assistant Leader*
B.B. Kosicki, *Assistant Leader*

Anderson, K.*	Geis, M.W.	Nichols, K.B.
Astolfi, D.K.	Goodhue, W.D.	Pang, S.W.
Bales, J.W.*	Gray, R.V.	Parker, C.D.
Bennett, P.C.	Hollis, M.A.	Pichler, H.H.
Black, J.G.	Huang, J.C.M.	Rabe, S.
Bozler, C.O.	Johnson, K.F.	Rathman, D.D.
Brown, E.R.	LaFranchise, J.R.	Reinold, J.H., Jr.
Burke, B.E.	LeCoz, Y.L.*	Rothschild, M.
Calawa, A.R.	Lincoln, G.A., Jr.	Sedlacek, J.H.C.
Chen, C.L.	Lysczarz, T.M.	Smith, F.W.*
Chiang, A.M.	Mahoney, L.J.	Smythe, D.L., Jr.
Clifton, B.J.	Maki, P.A.	Sollner, T.C.L.G.
Cullen, P.A.*	Manfra, M.J.	Utarro, R.S.
Daniels, P.J.	Mathews, R.H.	Vera, A.
Doherty, C.L., Jr.	McGonagle, W.H.	Wilde, R.E.
Doran, S.P.	McIntosh, K.A.	Young, E.M.
Durant, G.L.	Melngailis, J.†	
Efremow, N.N., Jr.	Mims, V.A.†	
Felton, B.J., Jr.	Mountain, R.W.	

* Research Assistant

† Staff Associate

‡ Part Time

1. SOLID STATE DEVICE RESEARCH

1.1 ANALYSIS OF JUNCTION DEPTHS AND LATTICE POINT DEFECT INTERDIFFUSION COEFFICIENTS IN $Hg_{0.8}Cd_{0.2}Te$

A model for the interdiffusion of lattice defects in $Hg_{0.8}Cd_{0.2}Te$ is proposed and applied to experimental results. It is assumed that the electrical properties of state-of-the-art nominally undoped $Hg_{0.8}Cd_{0.2}Te$ are determined by native defects. The model has been used to derive an equation for the junction depth obtained when a Te-rich sample is diffused under Hg-saturation conditions at low temperatures. Calculations using the equation agree with experimental data for junction depth *vs* excess Te concentration, diffusion time, and temperature. The basic model, which employs a two-valued interdiffusion coefficient, was successfully applied to the Pb-salt defect diffusion problem.^{1,2} It is assumed that the electrically active native defects are a doubly ionized acceptor (the Hg vacancy) and a singly ionized donor (probably the Hg interstitial). It is also assumed that in n-type material the difference between the concentration of donor impurities N_D and acceptor impurities N_A is negligible compared with the concentration of donor native defects I_{Hg} , i.e., $|N_D - N_A| \ll I_{Hg}$. The model is applied to the diffusion of Hg into an initially Te-saturated p-type crystal, which contains Te in excess of the stoichiometric composition. The indiffusing Hg eliminates the excess Te, both by decreasing the concentration of Hg vacancies and by removing any second-phase Te precipitates that may be present.^{3,4} As shown schematically in Figure 1-1, the diffusion process results in the formation of an n-type skin containing excess Hg, with the n-p junction located where indiffusing donor lattice defects (probably Hg interstitials) annihilate outdiffusing acceptor lattice defects (predominantly Hg vacancies).

The model has been used to derive the following equation for the junction depth x_j :

$$\frac{x_j^2}{t} = \frac{\pi S D_{Hg}^*(C_{Te-sat}^*)}{0.78 C_{XTe} \left[1 + \frac{D_{Hg}^*(C_{Te-sat}^*)}{0.78 D_{Hg}^*(C_{Hg-sat})} \right]^2} \quad (1-1)$$

where t is the diffusion time and S is the Hg atom concentration in the solid ($1.2 \times 10^{22} \text{ cm}^{-3}$). C_{XTe} is the total concentration of excess Te in the solid, i.e.,

$$C_{XTe} = C_{Te-sat}^* + C_{Te}^{ppt} \quad (1-2)$$

in which C_{Te-sat}^* is the excess Te present in the $Hg_{0.8}Cd_{0.2}Te$ phase relative to the stoichiometric composition for Te-saturated conditions and C_{Te}^{ppt} is the excess Te present as second-phase Te precipitates. $D_{Hg}^*(C_{Te-sat}^*)$ and $D_{Hg}^*(C_{Hg-sat})$ are the Te- and Hg-saturated Hg self-diffusion coefficients, respectively.

The variation of x_j^2/t with reciprocal absolute temperature for selected values of C_{Te}^{ppt} has been calculated from Equation (1-1) using the fast-component Hg self-diffusion coefficients given by Chen *et al.*,⁵ the partial Hg-vapor pressure curves of Tung *et al.*,⁶ and the Te-saturated solidus data of Schaake.^{7,8} (The fast-component coefficients have been selected as the values of D^*

because these coefficients were found by Chen to vary significantly with Hg partial pressure.) The results are shown in Figure 1-2. The calculated curve for $C_{Te}^{ppt} = 10^{18} \text{ cm}^{-3}$ is in good agreement with the data of Jones *et al.*⁹ In addition, as shown in Figure 1-3, the calculated variation of t/x_j^2 with C_{XTe} ($\approx C_{Te}^{ppt}$) at 270°C agrees with the data of Schaake *et al.*¹⁰

The Te-saturated and high-temperature metal-saturated solidus data for $Hg_{0.8}Cd_{0.2}Te$ are shown in Figure 1-4. The Te-saturated data points are from References 7 and 8, while the Hg-saturated data points are from References 7, 9, 11, and 12. The solid line in Figure 1-4 is the low-temperature branch of the Hg-saturated solidus calculated from the proposed native defect model.¹³ For 200 to 270°C, the electron concentrations fall within the range of values measured for most state-of-the-art samples that have been Hg saturated.

According to the present model, along the low-temperature branch of the Hg-saturated solidus, the Hg concentration exceeds that at the stoichiometric composition, and the excess increases with increasing temperature. The model does not predict an upper temperature limit for this branch, i.e., a temperature above which the excess Hg concentration decreases. Obviously there is such a limit, since the experimental data show that at sufficiently high temperatures the solid phase is Te-rich along the Hg-saturated solidus. A more complete model will be required to calculate the high-temperature branch of this solidus.

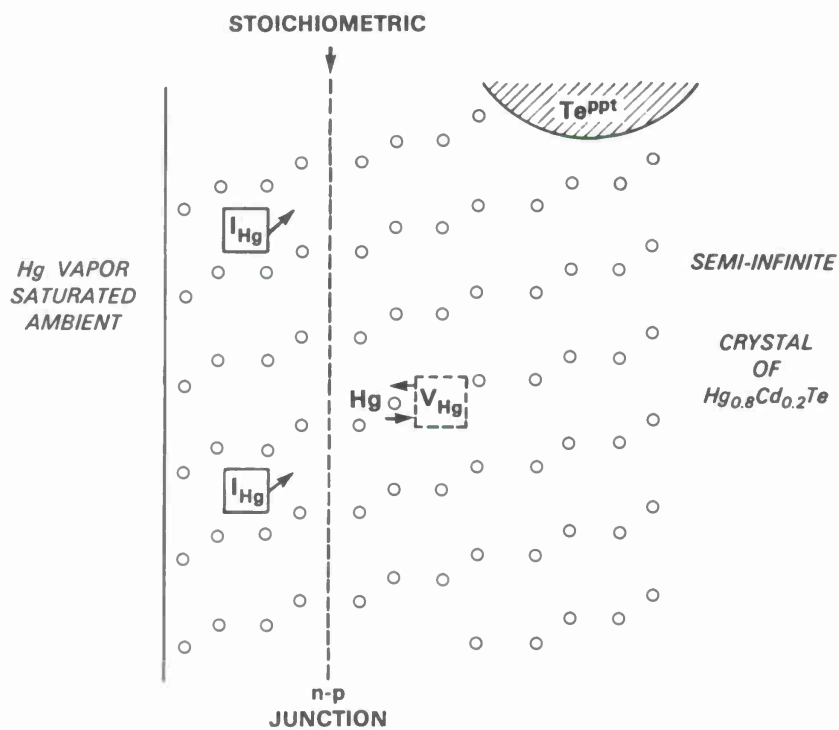


Figure 1-1 Schematic of model showing Hg interstitial, Hg vacancy, n-p junction, and part of a Te precipitate.

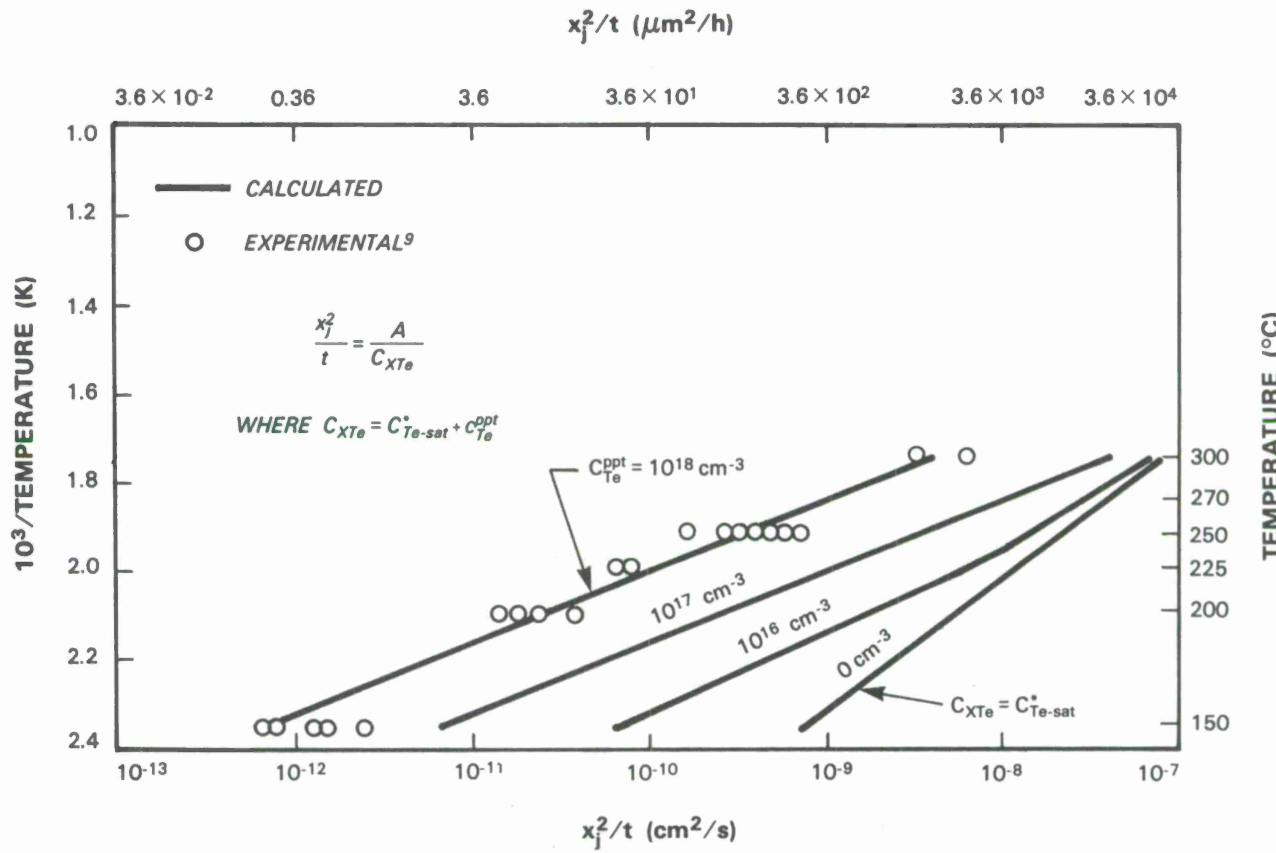


Figure 1-2 Ratio of $n-p$ junction depth squared x_j^2 to diffusion time t vs temperature.

The interdiffusion model also has been used to calculate the activation energies¹³ for the Hg-interstitial and Hg-vacancy interdiffusion coefficients, which are found to be 0.56 and 0.55 eV, respectively. The small activation energies and large magnitudes ($\approx 10^{-6} \text{ cm}^2/\text{s}$ at 270°C) of these coefficients are attributed to large atom jump frequencies due primarily to the weak Hg-Te bond.^{14,15}

In conclusion, for the first time a theoretical model has been found which fits $n-p$ junction diffusion data for nominally undoped $\text{Hg}_{0.8}\text{Cd}_{0.2}\text{Te}$ over a range of temperatures and excess Te concentrations. Furthermore, the model is consistent with most low-temperature Hg-saturation annealing experiments.

T. C. Harman

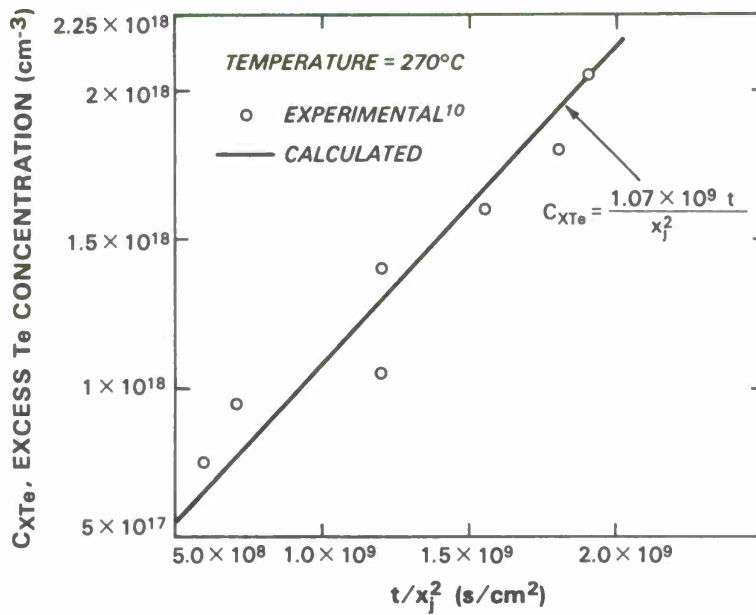
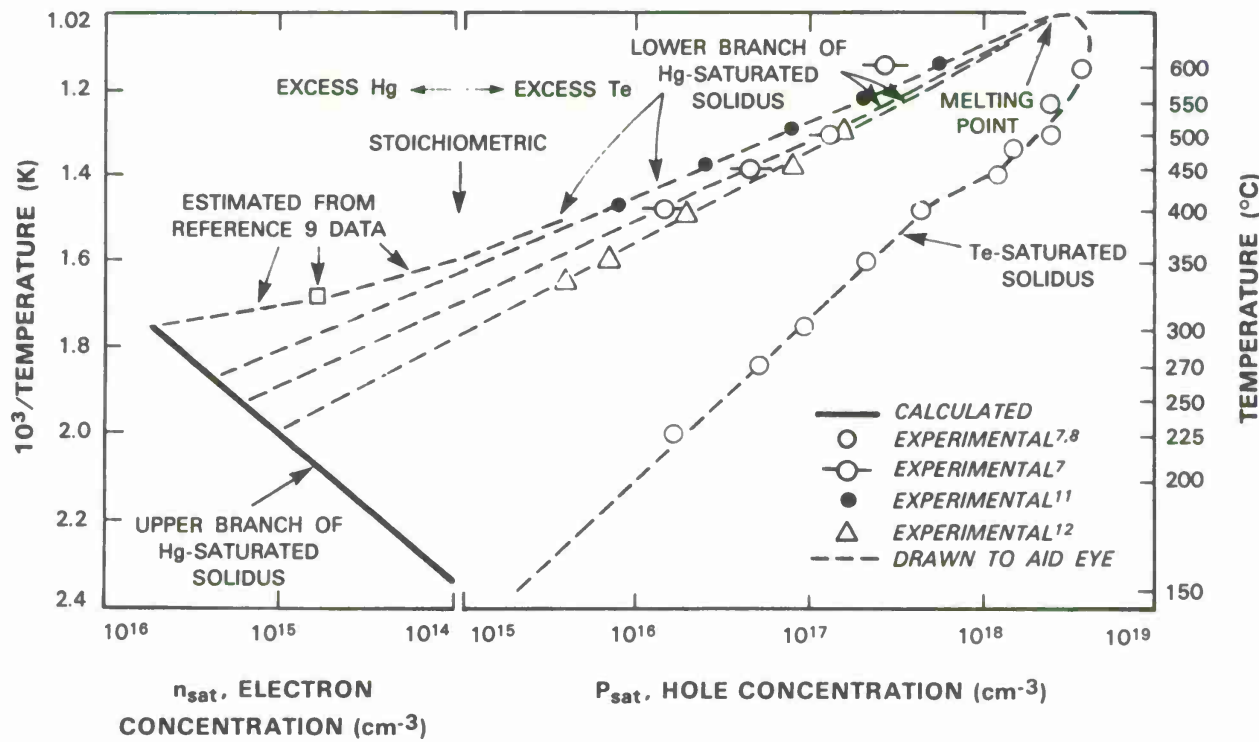


Figure 1-3 Ratio of diffusion time to n-p junction depth squared vs excess Te concentration.

80537-3



80537-4

Figure 1-4 Extrinsic carrier concentration vs isothermal annealing temperature for $Hg_{0.8}Cd_{0.2}Te$.

1.2 CAPLESS RAPID THERMAL ANNEALING OF $^{28}\text{Si}^+$ -IMPLANTED InP

Although good activation of most n- or p-type dopants implanted into InP can be achieved by conventional annealing at 750°C for several minutes,¹⁶ rapid thermal annealing (RTA) of InP, utilizing either high-intensity lamps or low-mass graphite heater strips, is becoming an attractive alternative. It has been reported¹⁷⁻²⁰ that several dopants exhibit minimal redistribution during RTA and that carrier concentrations and mobilities as good or better than those obtained by conventional methods can be achieved. For both conventional and RTA techniques, surface decomposition due to preferential P evaporation must be prevented by the use of a suitable dielectric encapsulant,^{16,21} careful control of the environment,²² or utilization of a close-contact proximity scheme.^{23,24} Although suitable encapsulant technologies have proven successful, a reliable capless annealing technique would simplify processing requirements and eliminate reproducibility problems sometimes encountered with thin encapsulating layers at higher anneal temperatures (>800°C).

In this report we present electrical activation results for $^{28}\text{Si}^+$ -implanted InP that has been heat-treated in a flash-lamp RTA system using an enhanced-overpressure proximity (EOP) capless annealing technique. This technique is similar to that used by Armiento and Prince²⁵ for RTA of GaAs. The EOP method for InP is based on the same principle as the In-Sn-P liquid-solution method for eliminating surface degradation of InP substrates prior to epitaxy, proposed by Antypas,²⁶ and therefore should be superior to conventional proximity techniques because a substantially higher P partial pressure exists over the In-Sn-P solution than over InP (Reference 26). The new method is also less prone to problems arising from surface irregularities or particulate contamination than conventional proximity techniques.

For RTA applications, an Sn-coated InP source wafer is mounted ~0.4 mm from the face of the implanted sample with the aid of a low-mass graphite support ring, as illustrated in Figure 1-5. This configuration then is mounted on the Si support tray of the lamp annealing system with a second Si cover wafer employed to prevent backside P evolution from blackening the quartz annealing chamber. The temperature is recorded by a thermocouple bonded to a small piece of Si mounted adjacent to the EOP fixture. Because of the optical absorption differences between the Si monitor wafer and an InP sample, this temperature-measurement scheme can introduce a small systematic temperature error which is both time and temperature dependent.

For these experiments, high-resistivity ($\rho > 10^7 \Omega\text{-cm}$) Fe-doped InP crystals were cut into (100)-oriented wafers that were lapped and polished using a 1 percent Br-methanol solution. Samples cut from the wafers were free-etched in 0.5 percent Br-methanol prior to room-temperature ion implantation of 140-keV 10^{14}-cm^{-2} $^{28}\text{Si}^+$ ions. Preparation of the 1-in-diam. InP source wafer, prior to sample annealing, consisted of e-beam evaporation of a 1- μm Sn layer, followed by a 5-min 750°C preanneal employed to saturate the Sn layer with P. Isochronal anneals were carried out in the flash-lamp RTA system, under flowing N_2 , for several temperatures up to 900°C.

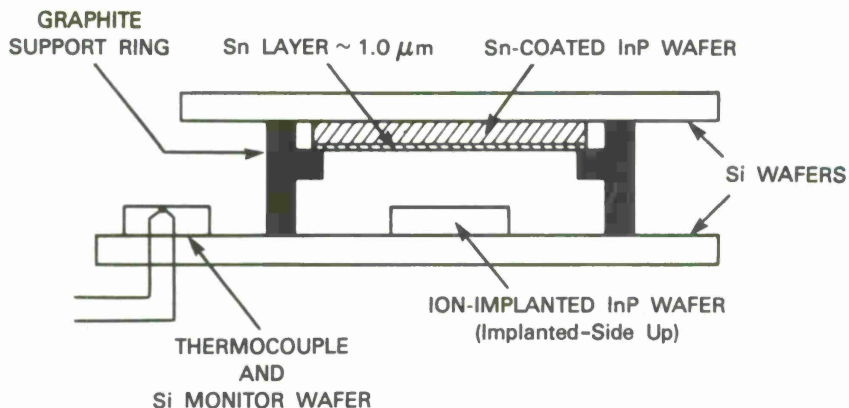


Figure 1-5 Schematic diagram of sample fixture used for EOP annealing technique.

Samples annealed by the EOP technique at 900°C for 10 s retained their mirror-like finish and, as shown in the photomicrograph of Figure 1-6(a), appear to have negligible surface pitting and are comparable to samples annealed with a PSG encapsulant at 750°C for 5 min [Figure 1-6(b)]. After approximately 15 annealing runs with the same source wafer, sample pitting began to occur and the wafer was replaced.

Although it has been reported that high levels of Sn were detected on the surfaces of InP substrates used for LPE growth while employing an In-Sn-P liquid solution preservation method,²⁷ Auger electron spectroscopy (AES) measurements performed on EOP-annealed InP wafers revealed that Sn surface contamination was undetectable within the measurement sensitivity of the apparatus. In order to investigate further the potential problem of Sn contamination during annealing, electrical measurements were performed on unimplanted EOP-annealed InP wafers (900°C for 10 s). These measurements showed that unimplanted InP wafers remained semi-insulating, again indicating that Sn contamination is not a problem.

The sheet carrier concentration, electron mobility, and resistivity of the implanted samples were determined by making Hall-effect measurements of the van der Pauw type.²⁸ The data in Figure 1-7 show that for a fixed anneal time, the sheet carrier concentration increases with increasing anneal temperature, and that the increase is greater for shorter anneal times. The highest sheet carrier concentration obtained, $6.7 \times 10^{13} \text{ cm}^{-2}$, was on a sample annealed at 900°C for 10 s. This value is considerably higher than that achieved on samples conventionally annealed at 750°C for 5 min, as illustrated in Figure 1-7 or reported elsewhere in the literature.²⁰ The measured sheet mobility of $1560 \text{ cm}^2/\text{V-s}$ obtained on the sample annealed at 900°C for 10 s is also an improvement over the mobility of conventionally annealed samples. A reduction of the 900°C anneal time to 3 s results in a reduction of both sheet carrier concentration and mobility. The general trend of increased sheet carrier concentration with increasing anneal time for all anneal temperatures is in good agreement with the results of Vaidyanathan *et al.*²⁰ for similarly

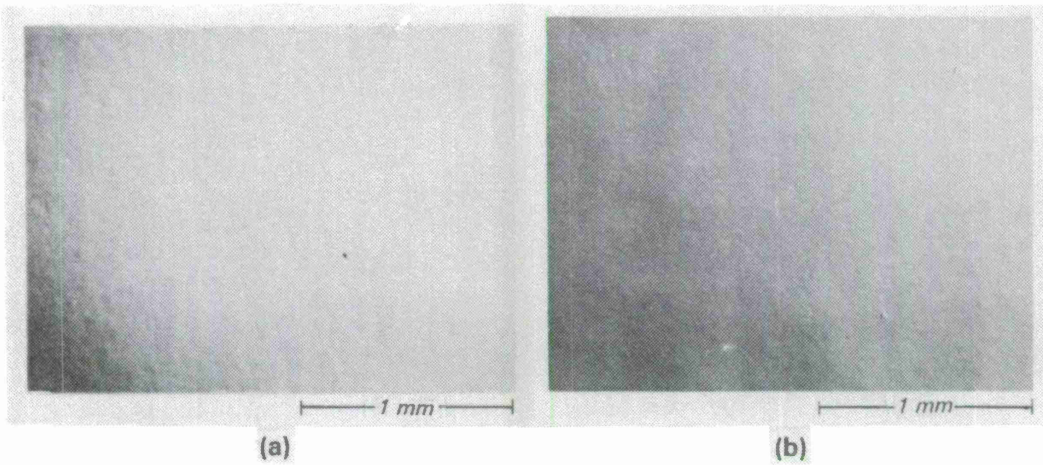


Figure 1-6 Photomicrograph of heat-treated InP surfaces: (a) EOP anneal at 900°C for 10 s; (b) conventional anneal using PSG encapsulant at 750°C for 5 min.

implanted samples. Our measurements, however, do not confirm their observation that a 750°C 20 s anneal produces a sheet carrier concentration comparable to that obtained with a conventional 750°C heat treatment. On the other hand, lower-dose implants will probably anneal by RTA at lower temperatures¹⁹ than these high-dose implants.

In all cases where a PSG encapsulant was employed, sheet carrier concentrations were slightly higher than the EOP results for the same anneal temperature. Although PSG encapsulation may prove superior for 750°C anneals, this film has not been able to withstand reproducibly the higher temperatures (900°C) required for obtaining maximum electrical activation.

J.D. Woodhouse J.P. Donnelly
M.C. Gaidis C.A. Armiento[†]

1.3 MEASUREMENT OF INTERMODULATION DISTORTION IN INTERFEROMETRIC MODULATORS

In a previous report,²⁹ it was shown that the dynamic range of analog optical-fiber communication links employing external optical modulators could be limited by modulator nonlinearities. Specifically, two-tone intermodulation distortion in interferometric modulators was analyzed. Here we present experimental results which verify these theoretical predictions.

[†] GTE Laboratories, Waltham, MA 02254

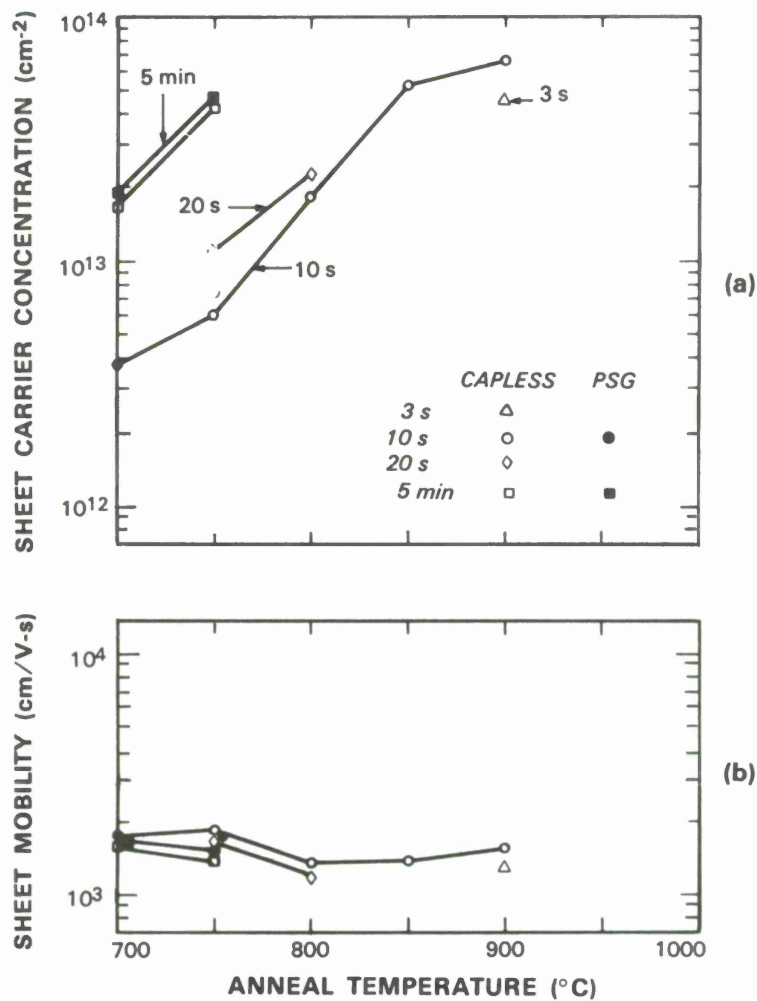


Figure 1-7 (a) Sheet carrier concentration and (b) sheet electron mobility vs anneal temperature for InP samples implanted with 140-keV 10^{14}-cm^{-2} Si^+ which were annealed using EOP and conventional techniques for several anneal times. Legend in (a) is applicable to (b).

The analog link we evaluated is shown in Figure 1-8 and consists of an optical source, an interferometric modulator, a photodetector, and an amplifier. The optical power transmission of the modulator varies sinusoidally with applied voltage. To analyze two-tone intermodulation distortion, it is assumed that the modulator drive voltage consists of two equal-amplitude sinusoidal signals and is given as

$$V_{in}(t) = V_I(\sin \omega_1 t + \sin \omega_2 t) \quad (1-3)$$

It is assumed that the device is operated with a phase bias of $\pi/2$ rad so that the transmitted power is approximately linear in applied voltage. In the analysis presented earlier,²⁹ it was shown that the detector output voltage can be written in series form as

$$V_{out}(t) = \sum_{k=1}^{\infty} V_{k,0} (\sin k\omega_1 t + \sin k\omega_2 t) + \sum_{k=1}^{\infty} \sum_{l=1}^{\infty} V_{kl} [\sin(k\omega_1 + l\omega_2)t + \sin(k\omega_1 - l\omega_2)t] \quad (1-4)$$

where the first and second summations correspond to harmonic and intermodulation frequencies, respectively. The coefficients $V_{1,0}$ and $V_{1,2}$ which correspond to the fundamental and dominant intermodulation signals, respectively, are proportional to the modulator drive voltage and are given by the expressions

$$V_{1,0} = 2V_o J_1\left(\frac{\pi V_I}{V_\pi}\right) J_0\left(\frac{\pi V_I}{V_\pi}\right)$$

$$V_{1,2} = 2V_o J_1\left(\frac{\pi V_I}{V_\pi}\right) J_2\left(\frac{\pi V_I}{V_\pi}\right)$$

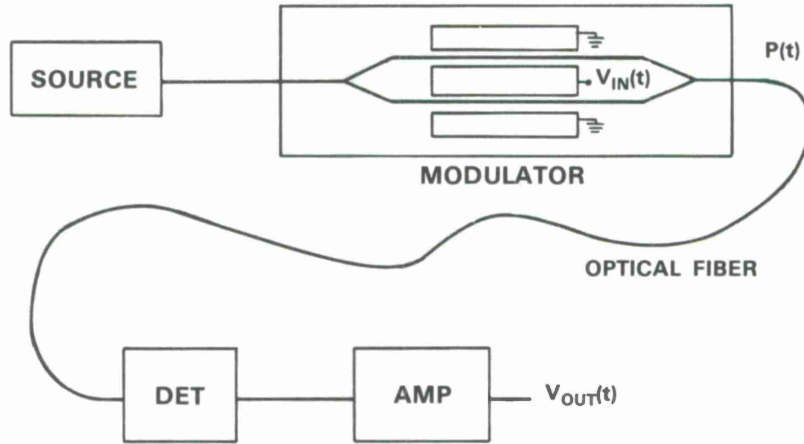
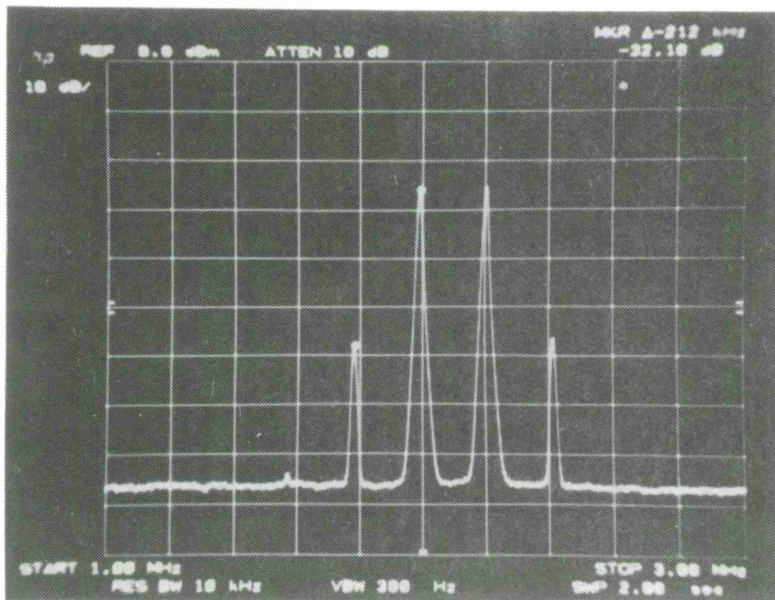


Figure 1-8 Analog optical-fiber communication link consisting of constant-power optical source, interferometric modulator, optical fiber, detector, and amplifier.

where V_o is one-half the peak value of V_{out} and J_n is the nth-order Bessel function. V_π is the voltage variation required for maximum on-off modulation corresponding to a phase shift of π rad between the two arms of the interferometer.

Intermodulation measurements were performed using an LiNbO_3 interferometric modulator designed for operation at an optical wavelength of $0.85 \mu\text{m}$. The device was tested using a GaAs diode laser and a Si photodetector. Equal-amplitude sinusoidal drive signals at frequencies of 2.0 and 2.2 MHz were simultaneously applied to the device. The amplified photodetector output signal was observed on a spectrum analyzer and the sideband levels were measured as a function of the drive-voltage amplitude. An example of a spectrum-analyzer trace is shown in Figure 1-9 for the case where $V_I/V_\pi = 0.16$. The two dominant signals at $\omega_1 = 2.0 \text{ MHz}$ and $\omega_2 = 2.2 \text{ MHz}$ can be seen with the two intermodulation signals at the frequencies $2\omega_1 - \omega_2 = 1.8 \text{ MHz}$ and $2\omega_2 - \omega_1 = 2.4 \text{ MHz}$. Intermodulation suppression is $\sim 32 \text{ dB}$ at this drive-voltage level. The complete set of experimental data along with the results of the theoretical analysis is plotted in Figure 1-10. The experimental data follow theoretical predictions very closely. There is a slight deviation from theory at the higher voltage levels and this likely is due to the fact that the induced electro-optic phase shifts in the modulator are not exactly linear with applied voltage. These measurements verify the limitations on system dynamic range resulting from intermodulation distortion. For example, to maintain $>40\text{-dB}$ intermodulation suppression requires that the input-voltage peak amplitude be $<0.09 V_\pi$.

L.M. Johnson



80537-7

Figure 1-9 Photograph of spectrum analyzer trace of amplified photodetector output for case where $V_I/V_\pi = 0.16$. Both fundamental and dominant intermodulation signals can be seen.

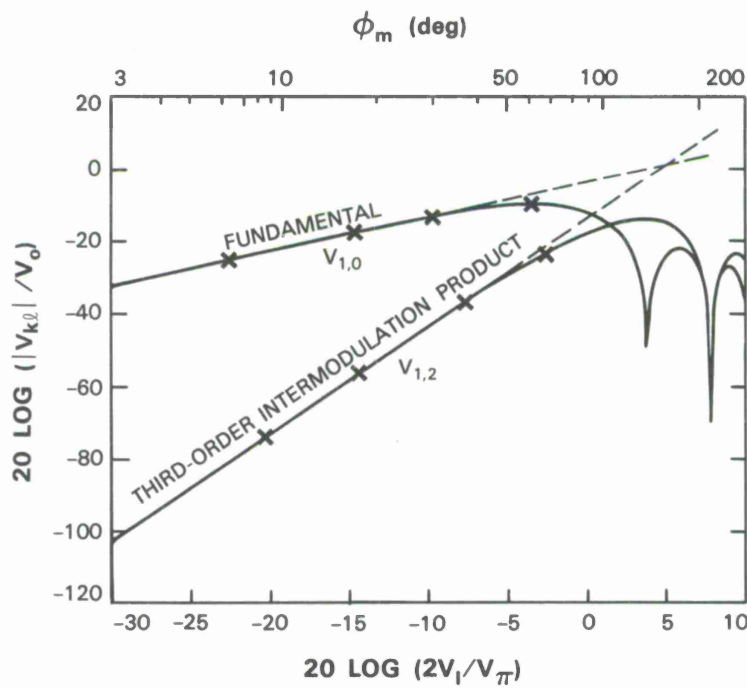


Figure 1-10 Plot of fundamental and intermodulation product power levels as a function of electrical drive power. Solid lines are theoretical predictions, with extrapolations to intermodulation intercept shown dashed; CROSSES are experimental results.

REFERENCES

1. R.W. Broderson, J.N. Walpole, and A.R. Calawa, *J. Appl. Phys.* **41**, 1484 (1970), DDC AD-710449.
2. R.L. Guldi, J.N. Walpole, and R.H. Rediker, *J. Appl. Phys.* **44**, 4896 (1973).
3. P.L. Anderson, H.F. Schaake, and J.H. Tregilgas, *J. Vac. Sci. Technol.* **21**, 125 (1982).
4. H.F. Schaake and J.H. Tregilgas, *J. Electron. Mater.* **12**, 931 (1983).
5. J.S. Chen, F.A. Kroger, and W.L. Ahlgren, Extended Abstracts of the 1984 Workshop on Physics and Chemistry of HgCdTe, San Diego, 15-17 May 1984.
6. T.Tung, C.-H. Su, P.-K. Liao, and R.F. Brebrick, *J. Vac. Sci. Technol.* **21**, 117 (1982).
7. H.F. Schaake, *J. Electron. Mater.* **14**, 513 (1985).
8. H.F. Schaake and J.H. Tregilgas, *J. Vac. Sci. Technol. A* **4**, 2181 (1986).
9. C.L. Jones, M.J.T. Quelch, P. Capper, and J.J. Gosney, *J. Appl. Phys.* **53**, 9080 (1982).
10. H.F. Schaake, J.H. Tregilgas, J.D. Beck., M.A. Kinch, and B.E. Gnade, *J. Vac. Sci. Technol. A* **3**, 143 (1985).
11. H.R. Vydyanath, *J. Electrochem. Soc.* **128**, 2609 (1981).
12. S.H. Shin and M. Khoshnevisan, Extended Abstracts of the 1984 Workshop on Physics and Chemistry of HgCdTe, San Diego, 15-17 May 1984.
13. T.C. Harman, unpublished.
14. T.C. Harman, M.J. Logan, and H.L. Goering, *J. Phys. Chem. Solids* **7**, 228 (1958).
15. W.E. Spicer, J.A. Silberman, I. Lindau, A.B. Chen, and J.A. Wilson, *J. Vac. Sci. Technol. A* **1**, 1735 (1983).
16. J.P. Donnelly and C.E. Hurwitz, *Appl. Phys. Lett.* **31**, 418 (1977), DDC AD-A050856/4.
17. A.N.M. Masum Choudhury, K. Tabatabaie-Alavi, C.G. Fonstad, and J.C. Gelpay, *Appl. Phys. Lett.* **43**, 381 (1983).
18. S.S. Gill and B.J. Sealy, *J. Cryst. Growth* **64**, 174 (1983).
19. D.L. Lile, D.A. Collins, and C.R. Zeisse, *IEEE Electron Device Lett.* **4**, 231 (1983).
20. K.V. Vaidyanathan and H.L. Dunlap, *Mat. Res. Soc. Symp. Proc.* **23**, 687 (1984).

21. D.E. Davies, J.P. Lorenzo, and T.G. Ryan, Solid-State Electron. **21**, 981 (1984).
22. D.E. Davies, W.D. Potter, and J.P. Lorenzo, J. Electrochem. Soc. **125**, 1845 (1978)
23. B. Molnar, Appl. Phys. Lett. **36**, 927 (1980).
24. C.W. Farley and B.G. Streetman, J. Electrochem. Soc. **134**, 498 (1987).
25. C.A. Armiento and F.C. Prince, Appl. Phys. Lett. **48**, 1623 (1986).
26. G.A. Antypas, Appl. Phys. Lett. **37**, 64 (1980).
27. B.H. Chin, G.P. Schwartz, W.C. Dautremont-Smith, and J.R. Dick, J. Electrochem. Soc. **133**, 2161 (1986),
28. L.J. van der Pauw, Philips Res. Rep. **13**, 1 (1958).
29. Solid State Research Report, Lincoln Laboratory, MIT (1986:2), p. 1.



2. QUANTUM ELECTRONICS

2.1 STABLE SINGLE-FREQUENCY $\text{Ti:Al}_2\text{O}_3$ RING LASER

Output from a single-frequency $\text{Ti:Al}_2\text{O}_3$ ring laser of at least 100 mW has been obtained between 740 and 820 nm, as shown in Figure 2-1. At the peak of the tuning curve the output was as high as 200 mW. The dip in the tuning curve near 800 nm was caused by the optics. The tuning range was limited by the bandwidth of the output coupler and the available power. In this experiment, the $\text{Ti:Al}_2\text{O}_3$ rod was pumped using 7 W of 514.5-nm light from an Ar-ion laser; only 3.5 W were incident on the crystal of which only 2 were absorbed.

Figure 2-2 shows the frequency stability of the ring laser over a 5-min period. These data were obtained from the output of a confocal Fabry-Perot spectrum analyzer. The Fabry-Perot scanned over the transmission peak in 100 μs . The laser frequency was recorded every 3 s with an accuracy of 4 MHz as shown in Figure 2-2. The rms frequency jitter obtained from this data was 15 MHz. In addition, the stainless steel mounting board for the laser expanded with time because of a slow temperature rise under pumping conditions, resulting in the observed long-term frequency drift of 270 kHz/s.

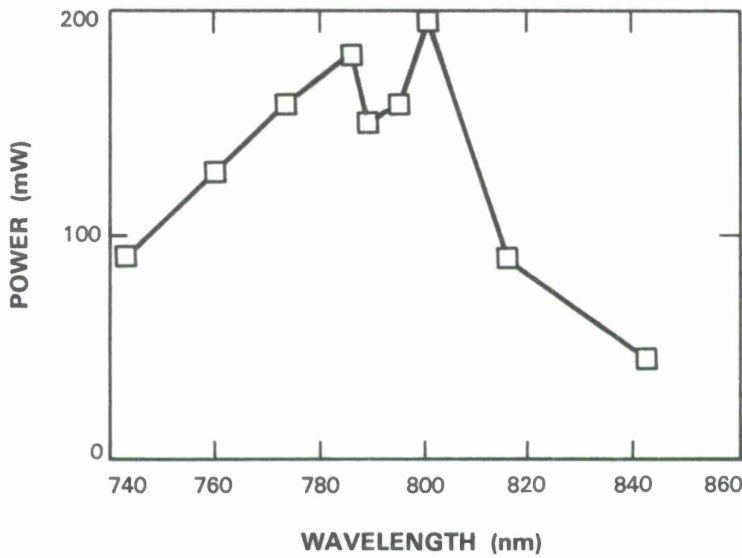


Figure 2-1 Single-frequency power vs wavelength. Output power of 100 mW can be obtained over 100-nm wavelength range with a maximum output power of 200 mW. Dip in middle is caused by laser cavity optics.

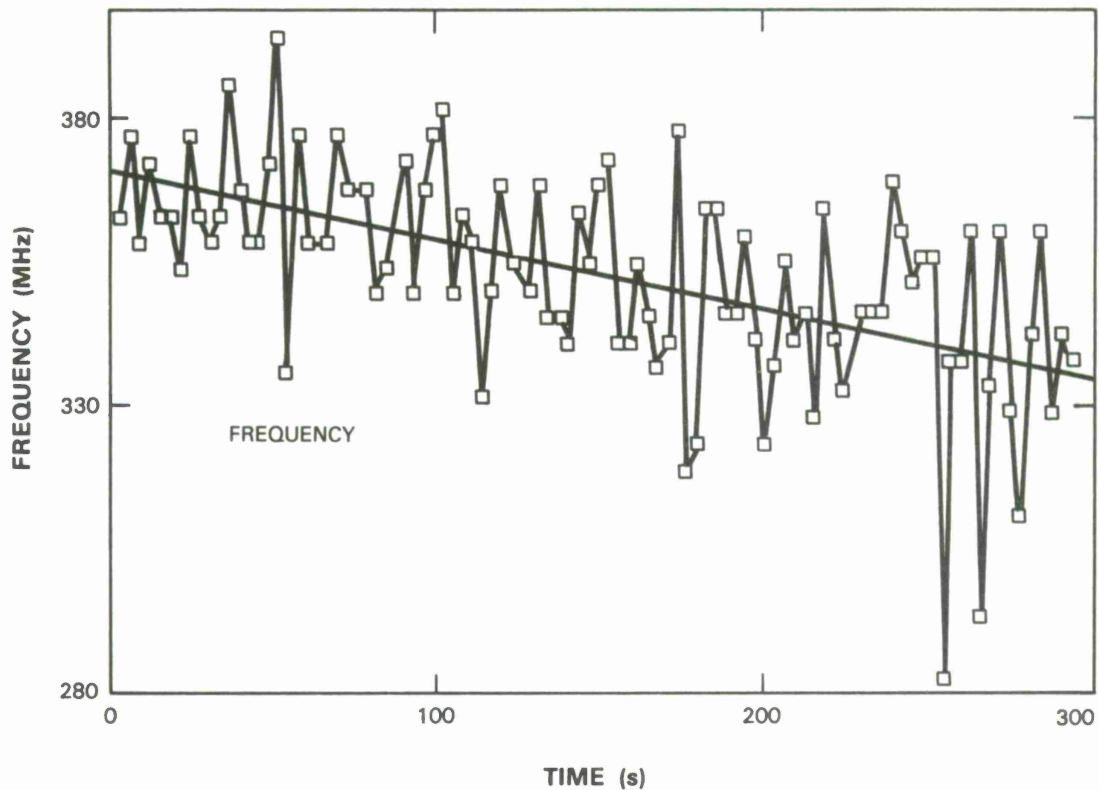


Figure 2-2 Frequency changes in 5 min. A least-squares linear fit of frequency is indicated.

Both the Ti:Al₂O₃ laser frequency jitter and the Ar-ion laser power showed fluctuations at a frequency around 200 Hz, indicating that the two were correlated. The Ar-ion laser power affects the temperature and refractive index of the Ti:Al₂O₃ crystal. A simple model predicts that a one-percent Ar-ion laser-power fluctuation causes 0.5-K temperature fluctuation in the crystal, which results in an optical path fluctuation in the laser cavity and a corresponding frequency fluctuation of 40 MHz. We expect the model to be reliable only as an order of magnitude estimate. In the model, the temperature rise in the pumped filament is assumed to be decoupled from the temperature rise of the bulk crystal, which should be a reasonable approximation on the 5-ms time scale of the pump fluctuations. Further evidence for this model is that frequency tuning of the Ti:Al₂O₃ laser occurs when the Ar-ion laser power is changed.

Heating the laser crystal causes an aberrated thermal lens in addition to changing the optical path of the laser cavity. Any lens placed in the laser cavity should affect the cavity mode; however, placing the lens at a beam waist minimizes the effect. Figure 2-3 shows the effect of the Ti:Al₂O₃ crystal position on the laser-power threshold. Data are taken by sweeping the Ar-ion laser power at a modulation frequency of 30 Hz and determining the intercept for the output laser power (the threshold). Moving the crystal is equivalent to moving the thermal lens along

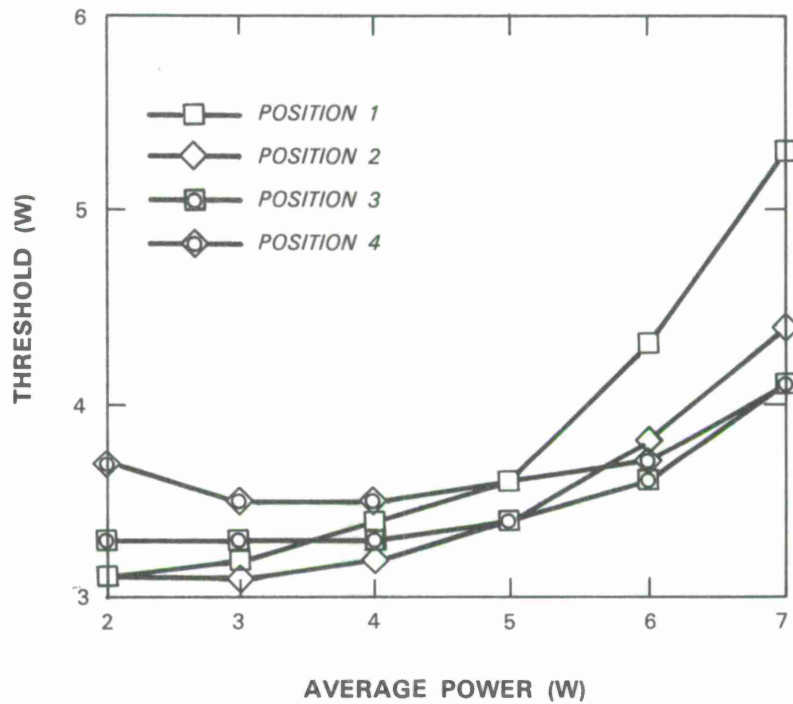


Figure 2-3 *Ti:Al₂O₃ laser threshold vs Ar-ion pump laser power for four different positions of Ti:Al₂O₃ crystal.*

the cavity. For changes in crystal position of 2 mm, there is a wide range of behaviors. For position 1, a strong effect of average power on the threshold is observed. For position 3, very little effect is observed, suggesting that at this position the Ti:Al₂O₃ crystal is centered on the beam waist. For other positions of the crystal, the power of the lens affects the laser threshold. This can be compensated for partially at any particular power, but not over a range of input power levels. At higher average power the threshold always increases. We believe this can be understood in terms of the Ar-ion laser mode structure, which tends toward a doughnut mode at high power.

In conclusion, 100-mW single-frequency output from a Ti:Al₂O₃ laser over the range 740 to 820 nm has been achieved. Thermal effects have been investigated. Ar-ion laser power affects Ti:Al₂O₃ crystal temperature, and thereby laser frequency. Jitter in the Ar-ion laser power causes a frequency jitter of the Ti:Al₂O₃ laser. The Ti:Al₂O₃ crystal also acts as an aberrated thermal lens, but this effect can be minimized by appropriately positioning the Ti:Al₂O₃ crystal.

P.A. Schulz
 D.J. Sullivan
 S. McClung

2.2 Nd:YAG SUM-FREQUENCY GENERATION OF SODIUM RESONANCE RADIATION

We previously reported¹ the generation of sodium resonance radiation by sum-frequency mixing the output radiation of a 1.064- and a 1.319- μm Nd:YAG laser. Recently we achieved a much higher mixing efficiency with two simultaneously Q-switched Nd:YAG lasers. In addition, we have measured the tuning range of both the 1.064- and 1.319- μm Nd:YAG lasers.

Figure 2-4 illustrates the tuning range of both the 1.064- and 1.319- μm Nd:YAG lasers when operated continuously. By operating one laser at a vacuum wavelength of 1.064608 μm and the other at 1.319224 μm , the sum radiation has a vacuum wavelength of 0.589159 μm and is resonant with the sodium D₂ transition. As the arrows in Figure 2-4 show, 1.319224 μm is at the peak of the tuning curve for the 1.319- μm Nd:YAG laser, while 1.064608 μm is near the peak of the tuning curve of the 1.064- μm Nd:YAG laser. The relative operating frequencies of each Nd:YAG laser and the sum radiation are shown in Figure 2-5. The 1.064- μm laser operated on three cavity modes separated by 160 MHz, while the 1.319- μm laser operated on three cavity modes separated by 110 MHz. The resulting sum radiation consisted of nine frequencies within a bandwidth of 540 MHz.

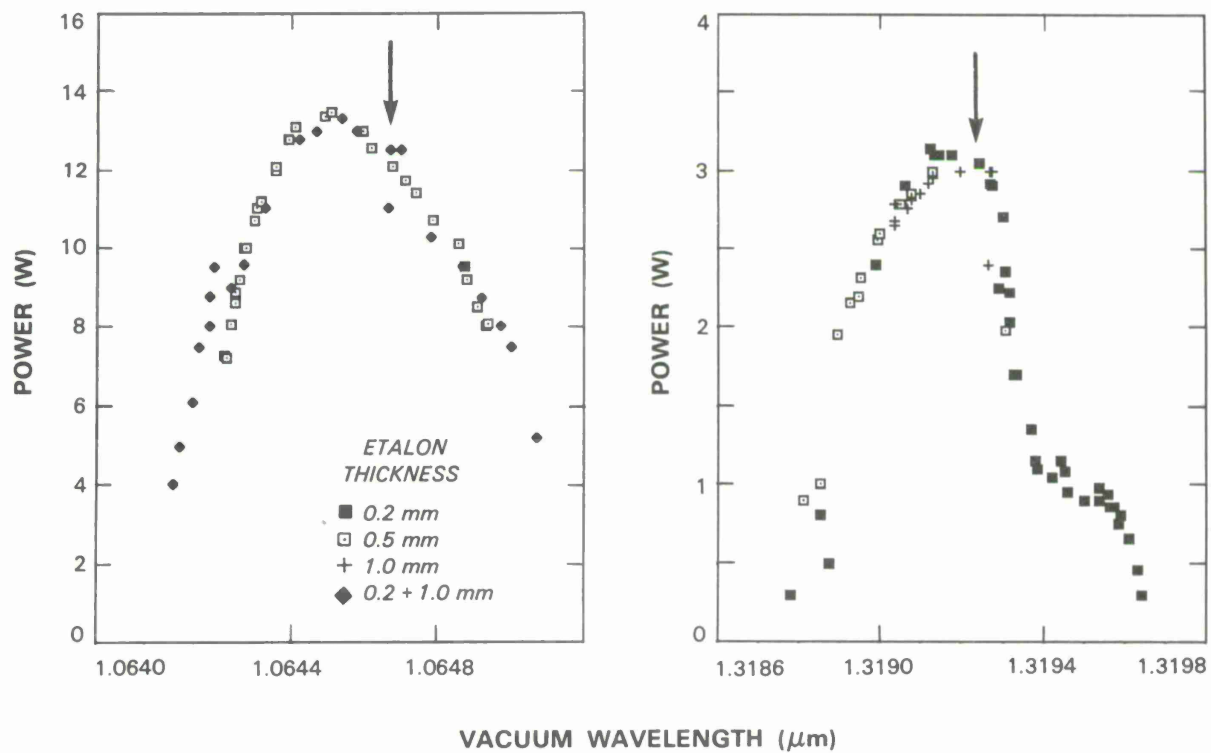


Figure 2-4 Tuning curves of 1.064- and 1.319- μm continuous Nd:YAG lasers.

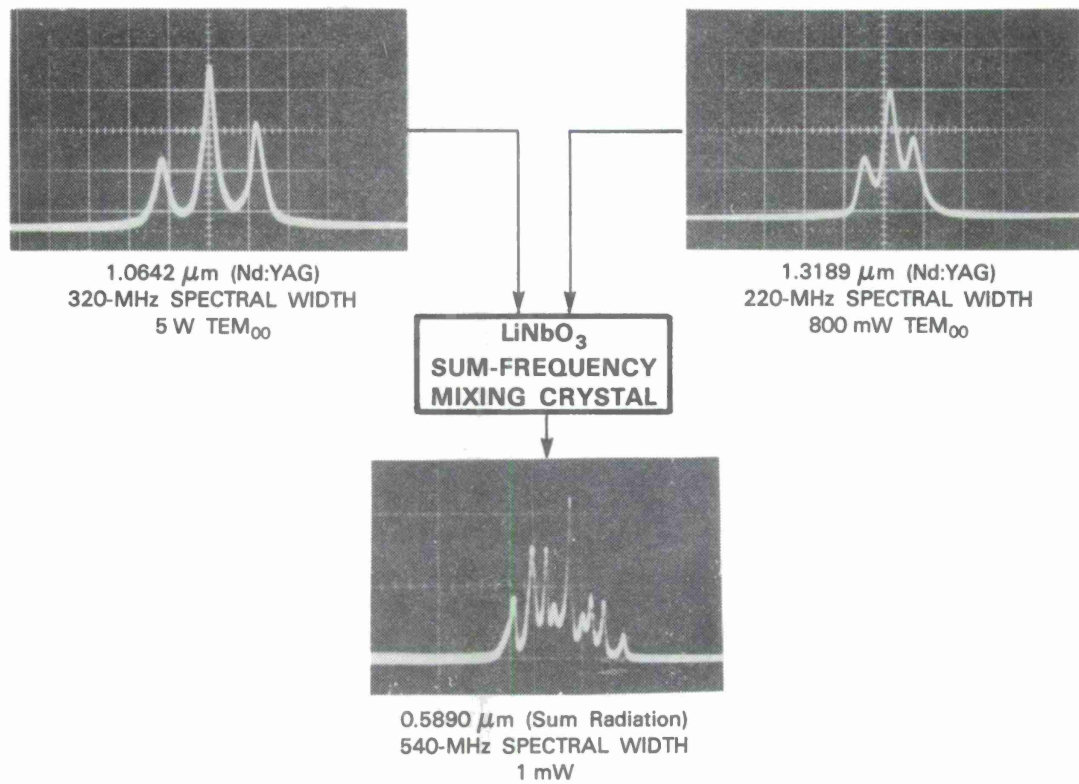


Figure 2-5 Spectral lineshapes of two continuous Nd:YAG lasers and corresponding sum-frequency radiation generated in a nonlinear crystal.

By simultaneously Q-switching each Nd:YAG laser, the peak powers of each were greatly enhanced, and thus mixing efficiency was increased. Figure 2-6 shows the temporal behavior of the pulsed radiation. When the Nd:YAG lasers were operated at a 2-kHz repetition rate, the 1.064- μm laser had an average output power of 5.9 W within a 1-GHz spectral range, while the 1.319- μm laser had an average output power of 1.6 W, also within a 1-GHz spectral range. The 0.589- μm radiation had an average power of 600 mW within a 2-GHz spectral range. The frequency mixing efficiency is 8 percent. As shown in Figure 2-6, the 1.064- μm pulse length of 80 ns is significantly shorter than the 1.319- μm pulse length of 250 ns. By lengthening the 1.064- μm pulse, we hope to achieve a much higher frequency-mixing efficiency.

T.H. Jeys A.A. Brailove
D.K. Killinger W.D. DeFeo

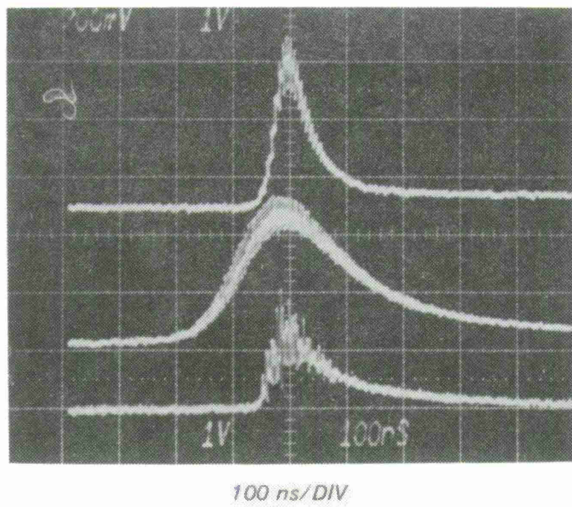


Figure 2-6 Upper and middle traces show shapes of 1.064- and 1.319- μ m Q-switched Nd:YAG lasers, respectively. Lower trace shows pulse shape of sum-frequency radiation.

2.3 NONLINEAR OPTICAL EFFECTS IN SEMICONDUCTOR COUPLED QUANTUM WELLS

The optical nonlinearities of semiconductor quantum-well (QW) structures hold promise for applications in integrated optoelectronic or photonic devices. For example, observation of saturable absorption in square QWs (Reference 2) has led to consideration of these structures for optical bistable devices.³ The recently observed optically induced blue shift of excitonic absorption⁴ also holds promise for applications in light-by-light switching. For these applications to be realizable, much larger nonlinearities are required.

We are exploring various mechanisms and structures in semiconductor heterostructures that may lead to these large optical nonlinearities. For example, coupled quantum wells⁵ (CQWs) are structures in which excitons have significantly larger electric dipole moments than in square QWs. A planar CQW in a heterostructure acts as a two-dimensional sheet having a large polarizability at frequencies near the exciton transition. Conceptually, such a planar structure is similar to a Langmuir-Blodgett film of organic molecules that has been shown to give rise to large optical nonlinearities.⁶ Figure 2-7 depicts two simple schemes for light-by-light modulation in these structures. In Figure 2-7(a), the interaction between a signal-carrier beam and a pump beam is realized via the optically induced CQW dipole field. Depending on whether or not the frequency of the signal beam is close to the excitonic absorption line, both amplitude and/or phase modulation are possible. This scheme also allows selective modulation depending on the polarization of the signal beam. Sideband generation is also possible if phase matching can be achieved. Figure 2-7(b) shows a slightly different mechanism for amplitude modulation. Since the electric field is perpendicular to the CQW dipole field, the only modulation mechanism is the shift of the excitonic absorption spectrum due to the optically induced CQW dipole field.

Figure 2-8 shows the transmittance spectra of a CQW sample that was studied previously.⁵ The solid curve shows the spectrum at low intensity, and the dashed curve, at high intensity. The major differences between the two spectra are a spectral shift of the excitonic line labeled (e_1, h_1) , and an increase of transmittance at the peak of the absorption line, as indicated in the figure. The increase of transmittance at the peak at higher intensity is believed to be the saturable absorption effect that is known to occur in bulk as well as QWs (Reference 2). However, the spectral shift of the exciton is due to a different phenomenon which we believe is the optically induced CQW dipole field depicted in Figure 2-7. Analysis of the dc Stark effect on this CQW structure⁵ predicts a blue shift of the (e_1, h_1) line on the order of ~ 1.1 meV for a reduction of the internal electric field by $\sim 0.4 \times 10^4$ V/cm. The sign and the magnitude of the observed spectral shift are consistent with the CQW model. Both effects, saturated absorption and spectral shift, result in light-by-light modulation with a depth up to 70 percent.

The mechanism for the results of Figure 2-8 involves the dipole field of real photogenerated carriers, which have a lifetime on the order of 1 ns. The result of a time-resolved study of the effect is shown in Figure 2-9, where the modulation of a weak optical signal pulse by an intense optical pump pulse is plotted as a function of the delay between the pump and signal pulses. Figure 2-9(a) shows a slow temporal decay of the shift on the order of 1 ns when the photon energy

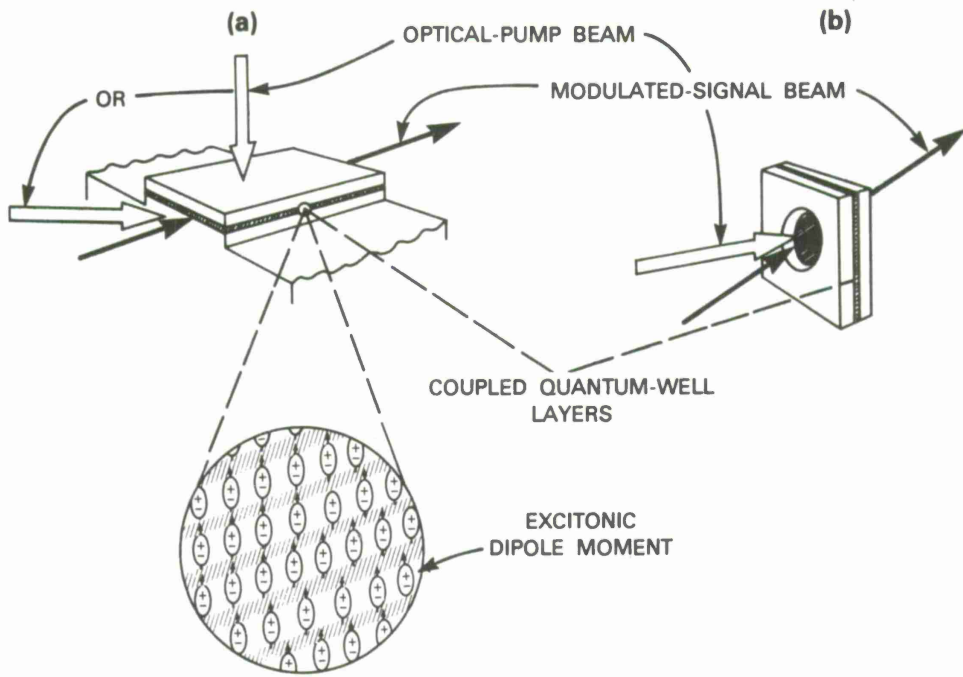


Figure 2-7 Schemes for light-by-light modulation. Signal beam can propagate either (a) parallel or (b) normal to CQW plane. Interaction occurs in CQW layers. Excitonic dipole moments are also symbolically shown.

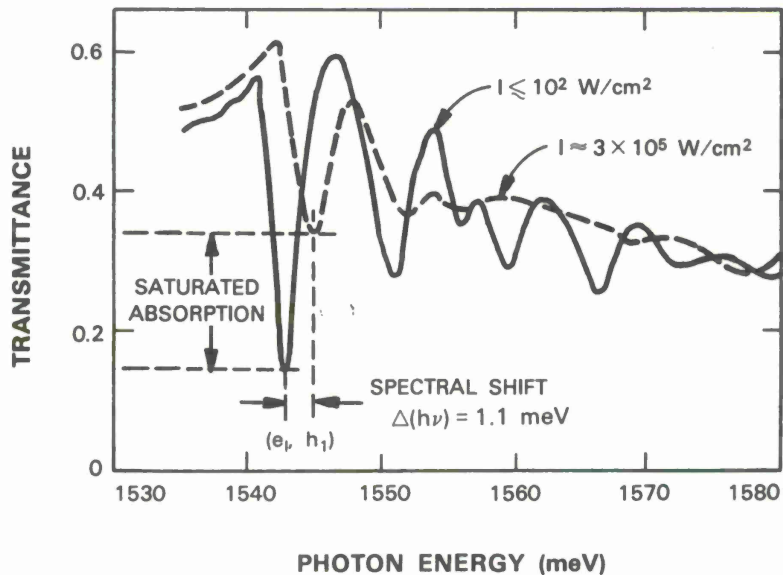


Figure 2-8 Evidence of change of CQW dipole moments induced by pump light. At high intensity, excitonic line labeled (e_1, h_1) blue shifts, which is consistent with a reduction in strength of internal electric field.

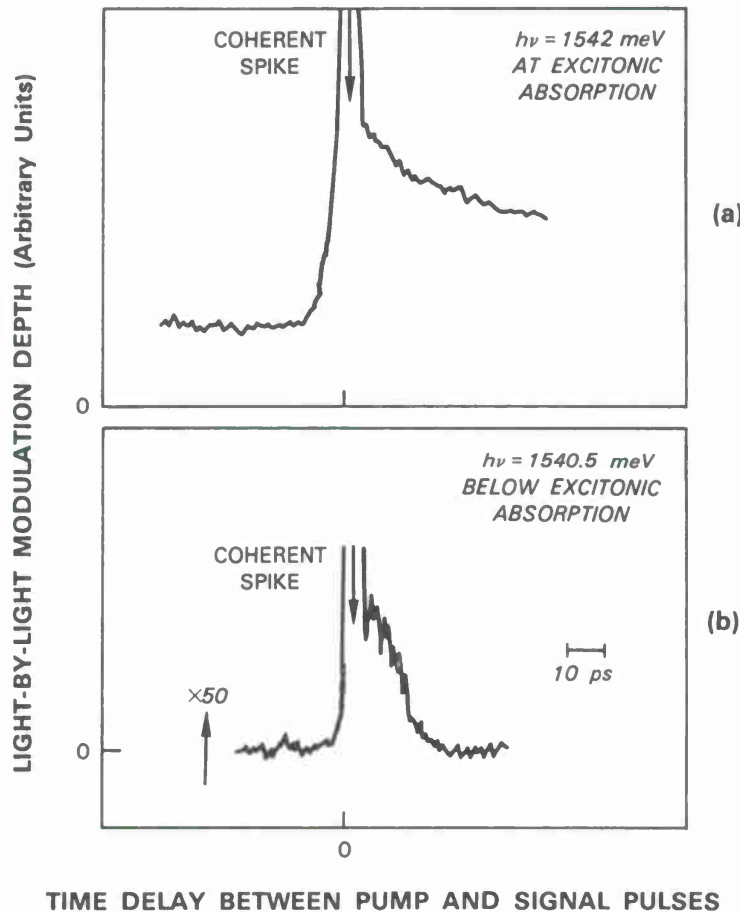


Figure 2-9 Time-resolved study of exciton blue shift shown in Figure 2-8. Modulation of a weak signal beam by an intense pump beam is measured as a function of delay between two pulses. (a) For pump excitation above exciton absorption line, carriers are generated, creating dipole screening which lasts for carrier lifetime. (b) For excitation below exciton transition, a faster effect is observed and interpreted as a result of virtual screening. Time resolution of measurement is 10 ps.

is above the excitonic line, and thus carriers are generated. As the photon energy is tuned to just below the excitonic edge, a faster effect that is about two orders of magnitude weaker is observed, as shown in Figure 2-9(b). We believe that the faster effect is the result of the screening of the internal electric field by virtual carrier excitation. Since the pump photons are not absorbed, the latter effect promises fast optical switching without significant dissipation of optical power.

H.Q. Le
J.V. Hryniewicz
J.J. Zayhowski

W.D. Goodhue
V.A. Mims

REFERENCES

1. Solid State Research Report, Lincoln Laboratory, MIT (1986:4), p.11.
2. D.A.B. Miller, D.S. Chemla, D.J. Eilenberger, P.W. Smith, A.C. Gossard, and W.T. Tsang, *Appl. Phys. Lett.* **41**, 679 (1982).
3. T. Venkatesan, B. Wilkens, Y.H. Lee, M. Warren, G. Albright, H.M. Gibbs, N. Peyghambarian, J.S. Smith, and A. Yariv, *Appl. Phys. Lett.* **48**, 145 (1986).
4. A. Mysyrowicz, D. Hulin, A. Antonetti, A. Migus, W.T. Masselink, and H. Morkoc, *Phys. Rev. Lett.* **56**, 2748 (1986).
5. Solid State Research Report, Lincoln Laboratory, MIT (1986:4), p.18.
6. See, for example, G. M. Carter in *Nonlinear Optical Properties of Organic Molecules and Crystals*, Vol. 2, edited by D.S. Chemla and J. Zyss (Academic Press, New York, 1987), pp. 85-120.

3. MATERIALS RESEARCH

3.1 MICROWAVE MESFETs FABRICATED IN GaAs LAYERS GROWN ON SILICON-ON-SAPPHIRE SUBSTRATES

There has been long-standing interest in the possibility of growing high-quality heteroepitaxial layers of GaAs on insulating, low-loss substrates, with the objective of fabricating devices with better isolation and improved high-frequency performance. In addition, for certain applications it would be advantageous to fabricate GaAs-based optoelectronic devices on optically transparent substrates such as sapphire. Recently, Kasai, Nakai, and Ozeki¹ have reported fabrication of MESFETs in GaAs layers grown by organometallic vapor phase epitaxy on (0001) sapphire substrates. These devices have a transconductance of only 20 mS/mm for a gate length of 2.5 μm , and to obtain even this value required the use of GaAs buffer layers over 30- μm thick.

We have reported previously² the fabrication of high-speed photoconductive detectors in GaAs layers grown by molecular beam epitaxy (MBE) on silicon-on-sapphire (SOS) substrates. These layers are superior in crystal quality to GaAs layers grown directly on sapphire because growth on the thin ($\sim 0.5\text{-}\mu\text{m}$) Si layer can be carried out by the well-established technique that is used for growing device-quality GaAs on bulk Si substrates and also because the lattice mismatch between GaAs and Si is only ~ 4 percent, compared with ~ 13 percent between GaAs and sapphire.

Now we have fabricated microwave MESFETs in GaAs layers grown by MBE on SOS substrates. For these monolithic GaAs-on-SOS (MGSOS) devices (which have a gate length of 0.8 μm) the dc transconductance is 140 mS/mm, the maximum frequency of oscillation f_{max} is 20 GHz, and the current-gain cutoff frequency f_T is ~ 8 GHz. These are the first results reported for the microwave performance of GaAs devices on sapphire substrates.

The procedure previously reported³ for MBE growth of GaAs on bulk Si substrates was used to grow GaAs layers on sections of commercial 2-in-diam. SOS wafers, which have nominal sapphire and Si orientations of (1102) and (100), respectively. In preliminary experiments we found that growth on wafers from a batch stated by the vendor to be somewhat misoriented gave GaAs layers with better surface morphology and photoluminescence properties than those grown on wafers closer to the nominal orientation. All the results reported here were obtained for devices fabricated in layers grown on one of these misoriented substrates, for which the Si film was found to be misoriented by $\sim 2.5^\circ$ from (100) toward (120).

For MESFET fabrication three epitaxial GaAs layers were grown on the SOS substrate: an undoped buffer layer 2- to 3- μm thick; an n active layer (Si-doped, $3 \times 10^{17} \text{ cm}^{-3}$) 0.15- μm thick; and an n⁺ contacting layer (Si-doped, $3 \times 10^{18} \text{ cm}^{-3}$) 0.05- μm thick. The device design is shown schematically in Figure 3-1. The devices were fabricated by means of a 1- μm recessed-gate process similar to one we have reported⁴ for fabricating monolithic GaAs-on-Si (MGS) MESFETs on bulk Si wafers.

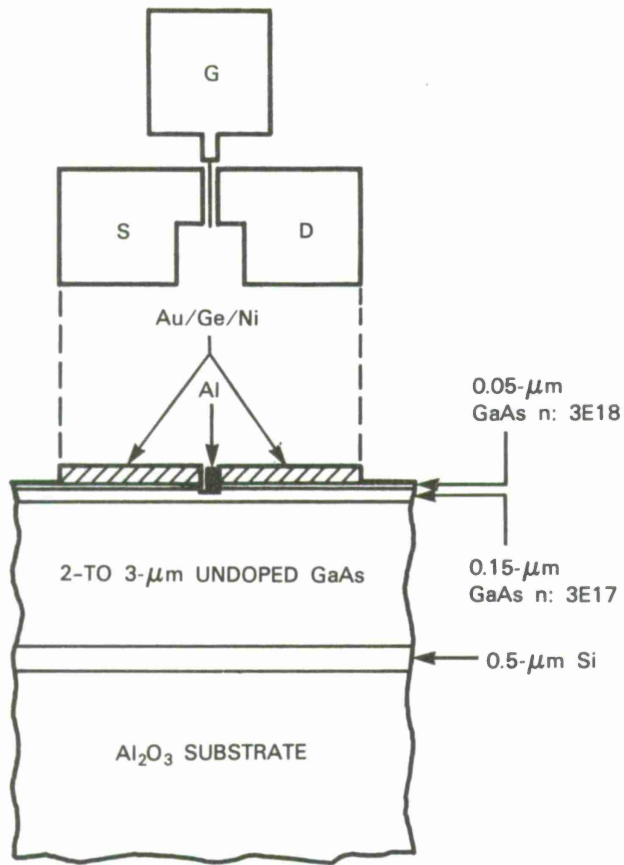


Figure 3-1. Schematic diagram of MGSOS microwave MESFET.

7956-1

Figure 3-2 shows the Schottky diode characteristic between the source and gate of our best MGSOS MESFET, for which the measured gate dimensions are $0.8 \times 40 \mu\text{m}$. The ideality factor is ~ 2 , compared with ~ 1.1 for our best MGS MESFET. The reverse leakage of the MGSOS device is $3 \mu\text{A}$ at -5 V , much higher than the value of $0.1 \mu\text{A}$ at -10 V obtained for the best MGS device. Figure 3-3 shows the low-frequency transistor characteristics of the same MGSOS MESFET. The transconductance measured at $V_{gs} = 0 \text{ V}$ is 140 mS/mm , compared with 150 mS/mm for our best MGS MESFET with a comparable gate length.

To characterize the microwave performance of the MGSOS MESFETs, a number of devices were mounted in microwave packages and the scattering parameters were measured over the range 2 to 26.5 GHz with a Hewlett-Packard 8510T network analyzer system. The maximum stable power gain (MSG), maximum available power gain (MAG), and current gain are plotted against frequency in Figure 3-4. From this plot we obtain $f_{\max} = 20 \text{ GHz}$ and $f_T \approx 8 \text{ GHz}$. For MGS MESFETs with comparable gate lengths, the highest reported f_T is 13.5 GHz, which was measured for devices with a gate width of $290 \mu\text{m}$ (Reference 5).

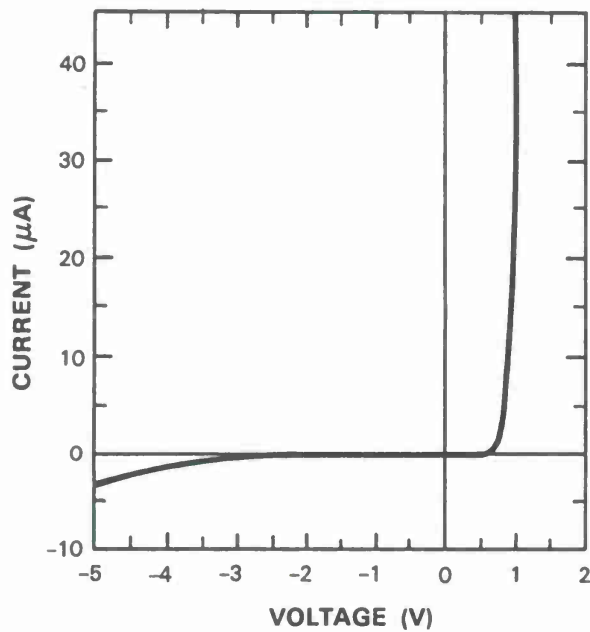


Figure 3-2. Gate Schottky diode characteristic of MGSOS microwave MESFET.

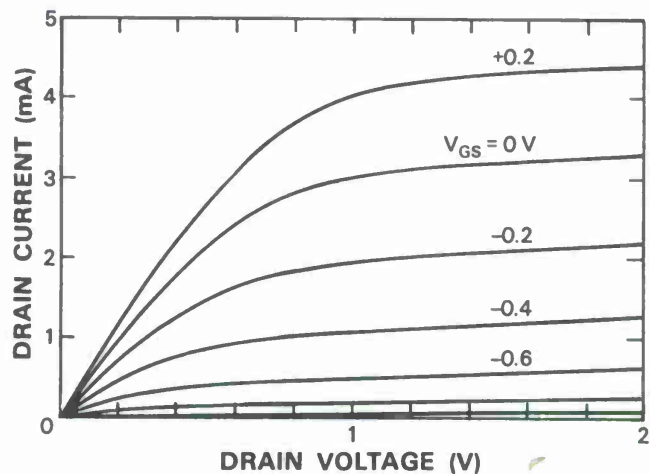


Figure 3-3. Transistor characteristics of MGSOS microwave MESFET with transconductance of ~ 140 mS/mm.

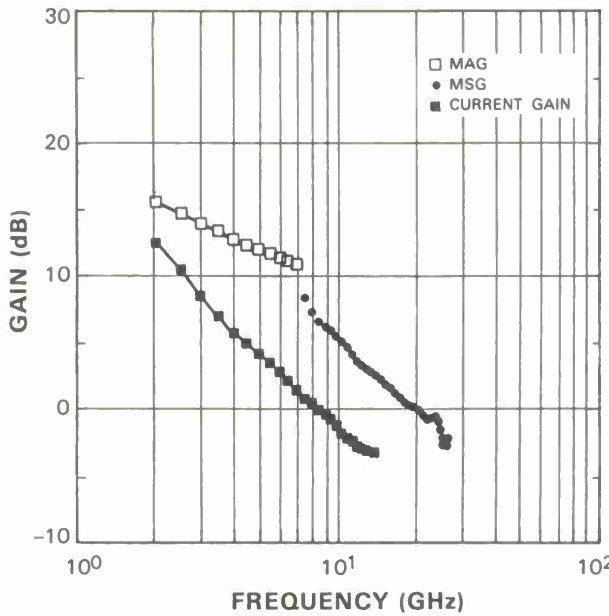


Figure 3-4. MSG, MAG, and current gain vs frequency for MGSOS microwave MESFET with $f_{max} = 20$ GHz and $f_T \approx 8$ GHz.

We believe that the Schottky diode and dc transistor characteristics of the MGSOS MESFETs are inferior to those of MGS MESFETs because the GaAs layers grown on SOS wafers have a higher defect density than those grown on bulk Si wafers. The GaAs-on-SOS layers exhibit lower low-temperature photoluminescence intensity and faster photoconductive decay than GaAs-on-Si layers.² These differences show that the GaAs-on-SOS layers contain a higher density of nonradiative recombination centers, which are presumably crystal defects. A higher defect density for the GaAs-on-SOS layers is not surprising, since the Si layers on which they are grown are greatly inferior in crystal quality to bulk Si wafers, which are essentially defect-free. A number of techniques, such as the solid phase epitaxy and regrowth (SPEAR) process,⁶ have been developed to improve the quality of SOS-Si layers. By using one of these techniques before GaAs growth, it should be possible to achieve a significant improvement in the GaAs-on-SOS layers, and therefore in the performance of the MGSOS MESFETs. It should be noted that the design of the present devices is not optimized for microwave performance because they were fabricated with a mask set used for processing MGS MESFETs operating at relatively low frequencies. Because their gate width is only 40 μ m, the MGSOS devices are more susceptible to degradation of their high-frequency performance by parasitic capacitances and inductances than are conventional microwave MESFETs, which have gate widths on the order of several hundred micrometers.

G.W. Turner
H.K. Choi
B-Y. Tsaur

3.2 OPTICAL ABSORPTION AND PHOTOLUMINESCENCE OF Ti:ScBO₃

The tunable Ti:Al₂O₃ laser was first demonstrated at Lincoln Laboratory in 1982.⁷ Laser action, which is due to Ti³⁺ ions, has been observed at wavelengths from 660 to 1060 nm (References 8, 9). Over most of this range, cw operation at room temperature¹⁰ has been achieved by using an Ar-ion laser for pumping the Ti³⁺ absorption band, which peaks at 490 nm. For a number of applications, it would be advantageous to find a host crystal in which this band is shifted to long enough wavelengths to permit pumping with diode lasers, for which the minimum output wavelength so far reported is 584 nm at 77 K (Reference 11). In view of the recent demonstration by Lai *et al.*¹² of tunable IR laser action in Cr:ScBO₃, together with the fact that TiBO₃ and ScBO₃ have the same crystal structure, we are investigating ScBO₃ as a possible host for Ti³⁺. In this report we present the results of optical absorption and photoluminescence measurements on single-crystal samples cleaved from a polycrystalline Ti:ScBO₃ boule grown by the thermal gradient-freeze technique previously used for Ti:Al₂O₃ crystals.¹³

Figure 3-5 shows the transmission spectrum measured with unpolarized light at room temperature for a 3-mm-thick sample from a boule prepared by solidifying a ScBO₃ charge doped with 0.7 wt% TiBO₃. The boule was light blue. To convert the transmission spectrum to an absorption spectrum, we have assumed that the observed maximum transmission of ~40 percent was limited by reflection and scattering losses. The absorption spectrum and a typical spectrum for Ti:Al₂O₃ are shown in Figure 3-6. Between ~480 and 760 nm there is a double-peaked absorption band, which by analogy with Ti:Al₂O₃ can be attributed to transitions between the ²T_{2g} ground state and the Jahn-Teller-split ²E_g excited state of the Ti³⁺ ion. The stronger and weaker peaks for Ti:ScBO₃ are located at 570 and 640 nm, respectively, compared with 490 and 540 nm for Ti:Al₂O₃. If it is assumed that the Ti³⁺ concentration is the same in the Ti:ScBO₃ sample as in the charge, the maximum absorption cross section is 3×10^{-21} cm², compared with 9.3×10^{-20} cm² for Ti³⁺ in Ti:Al₂O₃ (Reference 14).

For photoluminescence experiments, the Ti:ScBO₃ samples were pumped with 10-ns pulses of 532-nm radiation from a frequency-doubled Q-switched Nd:YAG laser. Preliminary observations (using color filters) indicate that the emission, like the absorption, is shifted to longer wavelengths than those found for Ti:Al₂O₃. Luminescence intensity was measured with a Si photodiode, with long-pass Corning-glass filters used to absorb pump radiation. In Figure 3-7, the intensity measured at 80 K for the sample of Figure 3-5 is plotted on a logarithmic scale against time. The data are fit by two straight lines with slopes corresponding to lifetimes of 0.85 and 1.8 μ s. Preliminary measurements indicate that the lifetime at 300 K is ~0.1 μ s, compared with ~3.1 μ s for Ti:Al₂O₃ at this temperature.^{8,9} In order to investigate the possibility that the lifetime has been reduced by impurities or concentration quenching, we plan to make additional measurements on samples from another Ti:ScBO₃ boule.

R.L. Aggarwal M.M. Stuppi
A. Sanchez A.J. Strauss
R.E. Fahey

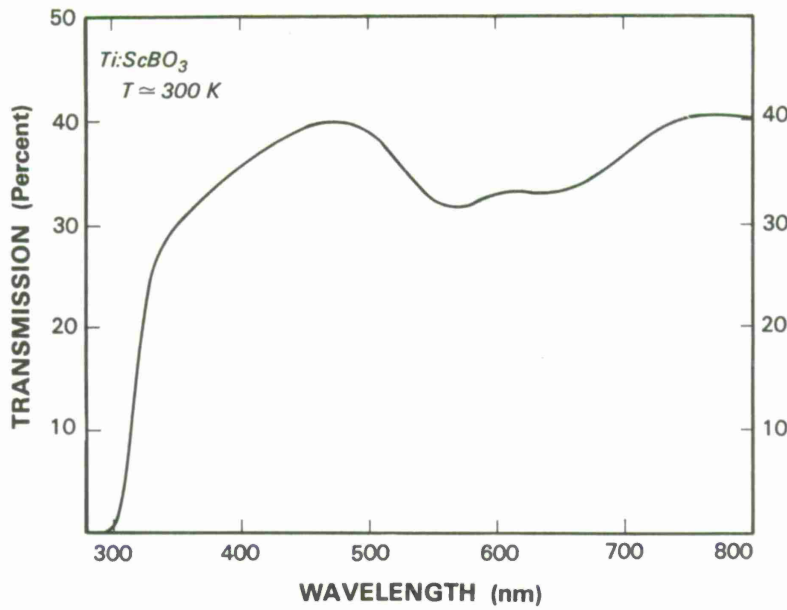


Figure 3-5. Transmission spectrum of a cleaved single-crystal sample of $Ti:ScBO_3$ at room temperature. Maximum transmission of 40 percent was limited by Fresnel losses and surface scattering.

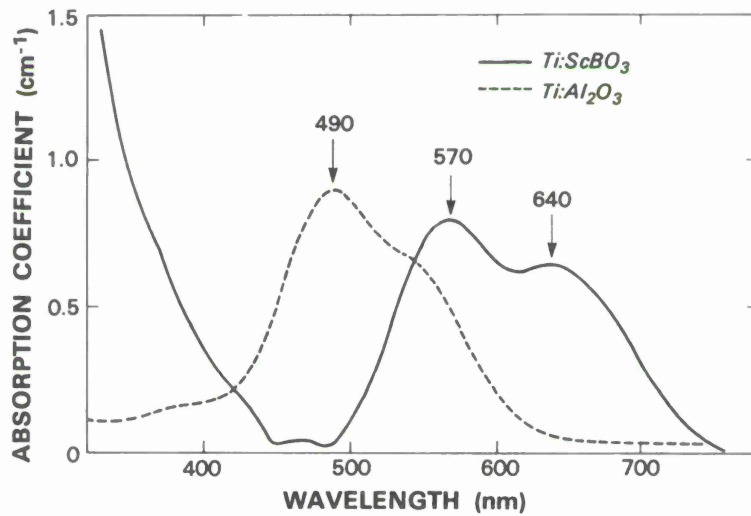


Figure 3-6. Absorption spectra at room temperature for $Ti:ScBO_3$ and $Ti:Al_2O_3$.

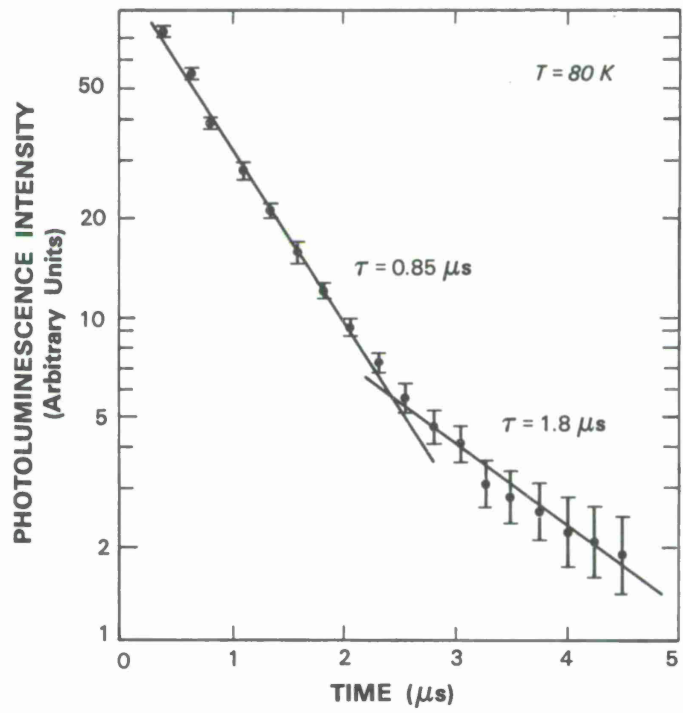


Figure 3-7. Photoluminescence intensity vs time for Ti:ScBO_3 at 80 K.

REFERENCES

1. K. Kasai, K. Nakai, and M. Ozeki, *J. Appl. Phys.* **60**, 1 (1986).
2. G.W. Turner, G.M. Metze, V. Diadiuk, B-Y. Tsaur, and H.Q. Le, *Conference Record 1985 IEEE International Electron Devices Meeting* (IEEE, New York, 1985), p. 468.
3. G.W. Turner, in *Semiconductor-Based Heterostructures*, ed. by M.L. Green *et al.*, (The Metallurgical Society, Warrendale, PA, 1986), p. 235.
4. H.K. Choi, G.W. Turner, B-Y. Tsaur, and T.H. Windhorn, *Materials Research Society Symposium Proc.* Vol. **67**, Palo Alto, California, 15-18 April 1986, p. 165, DTIC AD-A174740.
5. R.J. Fischer, N. Chand, W.F. Kopp, C-K. Peng, H. Morkoç, K.R. Gleason, and D. Scheitlin, *IEEE Trans. Electron Dev.* **ED-33**, 206 (1986).
6. D.C. Mayer, P.K. Vasudev, A.E. Schmitz, and R.E. Kastris, *Conference Record 1985 IEEE International Electron Devices Meeting* (IEEE, New York, 1985), p. 676.
7. Solid State Research Report, Lincoln Laboratory, MIT (1982:3), pp. 15-21, DTIC AD-A124305/4.
8. P.F. Moulton, *J. Opt. Soc. Am. B* **3**, 125 (1986).
9. P. Albers, E. Stark, and G. Huber, *J. Opt. Soc. Am. B* **3**, 134 (1986).
10. A. Sanchez, R.E. Fahey, A.J. Strauss, and R.L. Aggarwal, *Opt. Lett.* **11**, 363 (1986), DTIC AD-A170547.
11. I. Hino, S. Kawata, A. Gomyo, K. Kobayashi, and T. Suzuki, *Appl. Phys. Lett.* **48**, 557 (1986).
12. S.T. Lai, B.H.T. Chai, M. Long, and R.C. Morris, *IEEE J. Quantum Electron.* **QE-22**, 1931 (1986).
13. A.J. Strauss, R.E. Fahey, A. Sanchez, and R.L. Aggarwal, *Proc. SPIE* **681**, 63 (1986).
14. R.L. Aggarwal, A. Sanchez, R.E. Fahey, and A.J. Strauss, *Appl. Phys. Lett.* **48**, 1345 (1986).

4. MICROELECTRONICS

4.1 CCD SPATIAL LIGHT MODULATORS USING InGaAs/GaAs MULTIPLE QUANTUM WELLS

A monolithic CCD-addressed spatial light modulator (SLM) using electroabsorption effects in InGaAs/GaAs multiple quantum wells (MQWs) has been demonstrated successfully. A contrast ratio of 1.33 has been observed at 965 nm in a 16-stage CCD SLM.

The SLM structure is illustrated in Figure 4-1. The semiconductor layers were grown using molecular beam epitaxy (MBE) at 520°C on a semi-insulating GaAs substrate. In order of growth, the structure consisted of a p⁺ GaAs ground plane, the undoped InGaAs/GaAs MQW

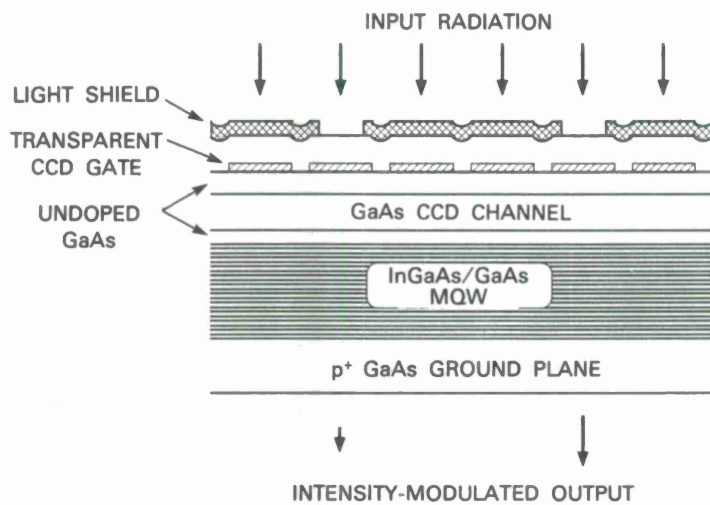


Figure 4-1. Cross section of a CCD SLM using an InGaAs/GaAs MQW structure.

structure, an undoped GaAs buffer layer, the n-type GaAs channel, and an undoped GaAs cap layer. The strained-layer MQW structure was composed of 60 periods of 15-nm-thick InGaAs QWs separated by 13-nm-thick GaAs barrier layers. The In concentration in the alloy was determined from flux measurements and secondary ion mass spectrometry (SIMS) to be 22 and 17 percent, respectively. The GaAs CCD channel was doped with Si to produce a carrier concentration of $5 \times 10^{16} \text{ cm}^{-3}$. The CCD channel thickness of 375 nm and the undoped surface layer of 312 nm were chosen to produce a pinchoff of $\sim 10 \text{ V}$ and to optimize the gate-to-gate breakdown voltage. The undoped GaAs layer between the InGaAs/GaAs superlattice and the GaAs CCD channel helps to prevent carriers in the MQW structure from reaching the CCD wells. Optical modulation occurs in the MQW layers when the electric field across these layers is modulated by

the charge in the CCD wells. One advantage of the GaAs/InGaAs system is that the GaAs substrate used for seeding the MBE growth of the device layers is transparent at 965 nm (the wavelength used in optical modulation measurements) and therefore does not need to be removed, in contrast to AlGaAs/GaAs-based modulators.¹

One-dimensional, 16-stage, 3-phase CCDs were fabricated on the GaAs surface of the SLM employing the planar-gate structure depicted in Figure 4-1. The gates consist of e-beam-evaporated W \sim 7.5-nm thick, and are \sim 9.5- μ m long with 1.5- μ m gaps between gates for the device reported here. The thin W has an optical transmission of \sim 0.5 at the wavelengths of interest. The metallization then is coated with 600-nm pyrolytic SiO₂. The channel width and length are defined using proton isolation, and ohmic contacts are formed to the n-type GaAs after etching away the undoped surface layer. A second metallization of Ti and thick Au is used to provide gate interconnects and bonding pads. Finally, a 50-nm-thick Al light shield is evaporated over two semitransparent phases and the gaps between devices to block the transmittance of unmodulated light through the device.

An example of the GaAs CCD electrical performance at a 1-MHz clock rate is shown in Figure 4-2. The input to the device is a sequence of 16 pulses (upper trace); the lower trace shows the delayed output. The lower amplitude of the first few output pulses is due to charge-transfer inefficiency. At present we are uncertain concerning the origin of this charge loss. One possibility may be the presence of potential pockets which form beneath the interelectrode gaps when such gaps are larger than \sim 1 μ m (Reference 2).

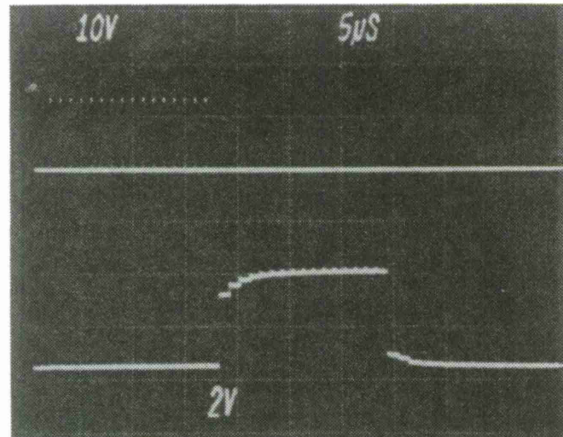


Figure 4-2. Electrical performance of a 16-stage CCD SLM at a 1-MHz data rate. Upper trace shows 16 sampling pulses applied to an input gate and lower trace is CCD output.

80537-22

Optical modulation was measured on this device before the light shield was deposited, and as a result the optical input signal was incident on all the gates simultaneously. The modulated optical signal was measured using a photomultiplier mounted below the GaAs substrate and the wavelength of the input signal was chosen to maximize the modulation. The contrast ratio (ratio of maximum to minimum transmission) of this device was 1.11 at 965 nm when the CCD channel voltage swing was 7 V. Since at any given instant only one phase holds the charge and is modulating the optical input, the contrast ratio of a single phase is at least 1.33. In addition, the gaps between gates are also not modulating the signal, so that the addition of a light shield may result in an even higher modulation.

K.B. Nichols B.F. Aull
W.D. Goodhue B.F. Gramstorff
B.E. Burke

4.2 SIMULATIONS OF Si PBT

A two-dimensional numerical simulation program (CANDE; Reference 3) has been used to aid in the optimization of key device parameters such as channel doping, grating periodicity, and epitaxial thickness for both Si PBT and Si VFET devices. This program solves the coupled Poisson and current-continuity equations and, therefore, is capable of generating the complete I-V characteristics for any unipolar device; the program also calculates capacitance and performs avalanche breakdown analysis, which is particularly important for high-power devices. A further feature of CANDE is the ability to input doping profile information from process simulation programs such as SUPREM 3. Results were obtained using CANDE for implanted Si PBT devices.

Figure 4-3 illustrates three different impurity profiles that have been used in simulations of the Si PBT. The distance parameter is measured along a vertical line through the center of a PBT device channel. The base grating is located 0.5 μm from the top of the device. The heavily doped n regions represent the substrate ($\geq 1.5 \mu\text{m}$) and a heavy, shallow As implant ($\leq 0.3 \mu\text{m}$) which form the collector and emitter regions, respectively, of the device. Profile 1 was obtained using an epitaxial layer uniformly doped with As at $4 \times 10^{16} \text{ cm}^{-3}$. P was implanted for channel implant profile 2 at an energy of 400 keV and a dose of $3.2 \times 10^{12} \text{ cm}^{-2}$. Profile 3 was obtained with a 300-keV P implant at a dose of $2.8 \times 10^{12} \text{ cm}^{-2}$. Both implants were followed by an anneal at 1000°C for 30 min. All of the profiles shown in Figure 4-3 were obtained using SUPREM 3 simulations, but their validity has been verified by SIMS analysis and C-V profiling.

Figure 4-4 compares the collector I-V characteristics obtained from CANDE for devices having impurity profiles 1 and 3. A higher output impedance and lower turn-on voltage is indicated for the 300-keV-implanted device compared with the uniformly doped device. Maximum transconductance for devices made from the two profiles is nearly equal even though the profiles in the collector regions are substantially different. The difference between profiles 2 and 3, shown in Figure 4-5, can be viewed essentially as a 1500- \AA shift in the channel implant with respect to the base grating location. This relatively small difference in profiles produces a large difference in

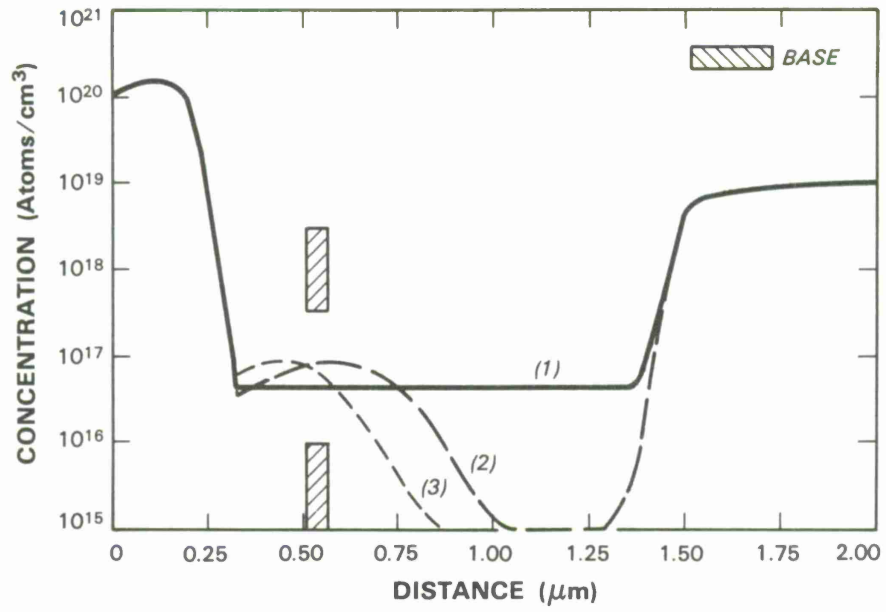


Figure 4-3. Three impurity profiles used in simulations of Si PBT: (1) uniformly As-doped epilayer; (2) 400-keV, $3.2 \times 10^{12} \text{-cm}^{-2}$ P implant; and (3) 300-keV, $2.8 \times 10^{12} \text{-cm}^{-2}$ P implant.

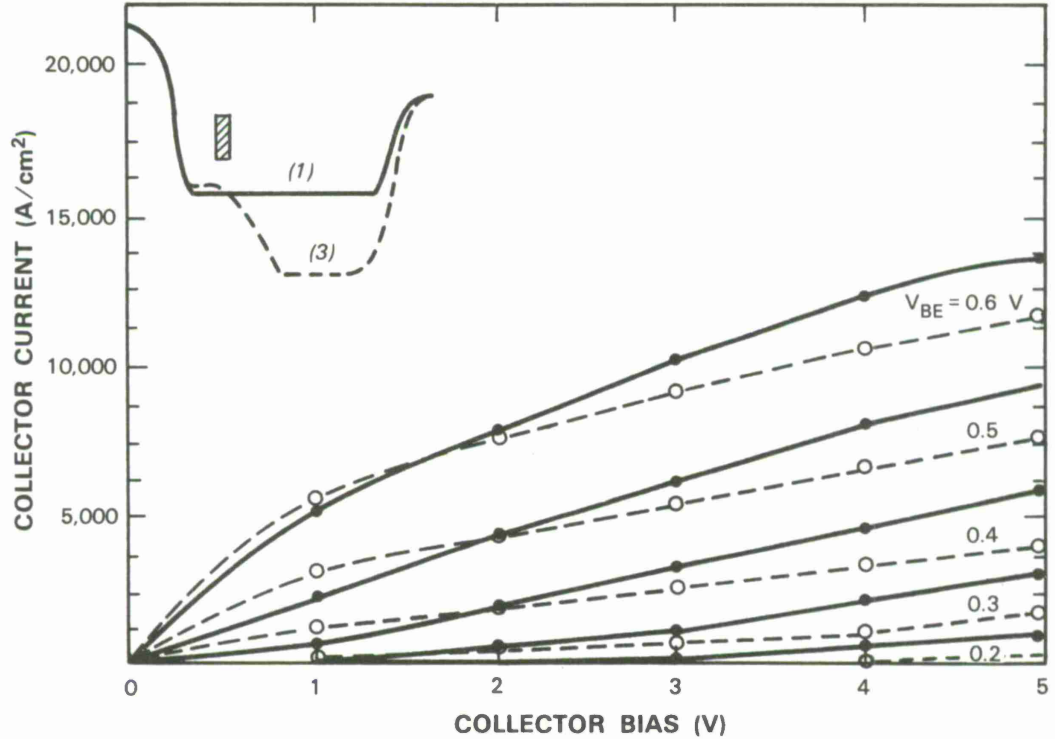


Figure 4-4. Simulated collector I-V characteristics for devices with profiles 1 and 3.

80537-23

80537-24

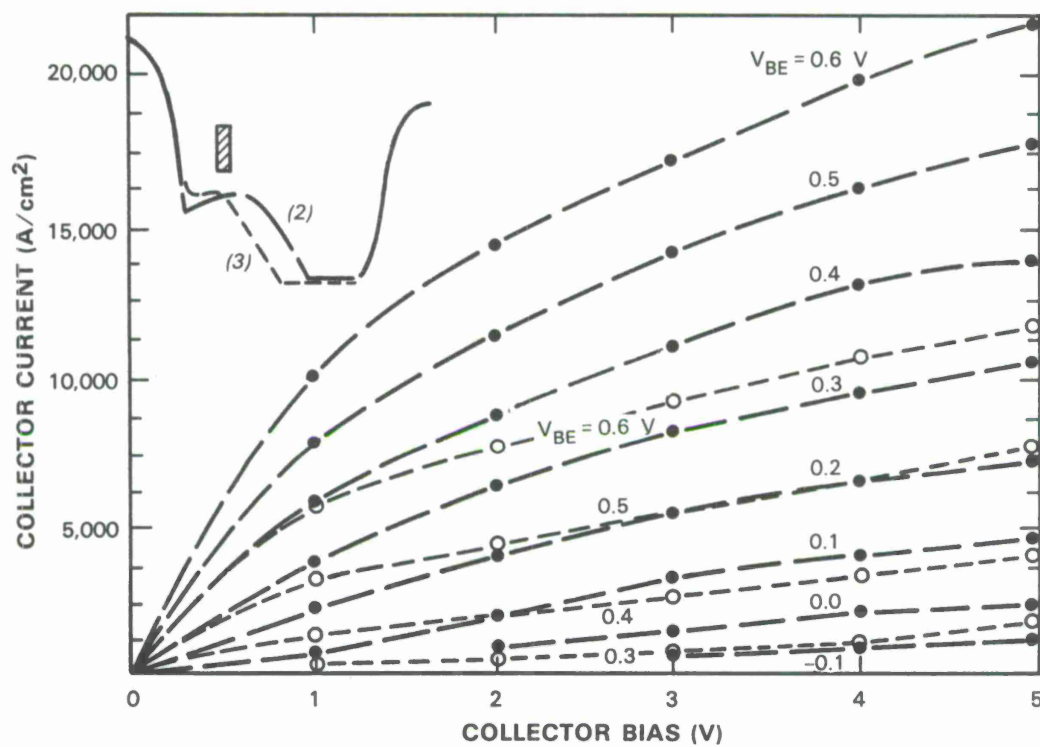


Figure 4-5. Simulated collector I-V characteristics for devices with profiles 2 and 3.

transconductance, threshold voltage, and current density. This demonstrates that the PBT is very sensitive to doping variations in the immediate vicinity of the base, and, therefore, channel doping, base grid spacing, base thickness, and base depth all must be known precisely in order to predict accurately actual device behavior.

Figure 4-6 shows a comparison of an experimental collector I-V characteristic with that obtained from CANDE for the device parameters shown in the figure. The simulated data were corrected for a base-emitter series resistance of 7Ω , which was obtained from an independent measurement. The fit is remarkably good, as CANDE accurately predicts threshold voltage, transconductance, current density, and output impedance for the experimental device. It even predicts the base bias for the maximum transconductance ($V_{BE} = 0.0$, fourth curve from the top). The base electrode for CANDE was simulated as a p-n junction since the program at present does not handle Schottky contacts. This introduces a base-voltage shift in the collector I-V characteristics equal to $E_g/2q - \phi_B$, but otherwise has no effect.

D.D Rathman

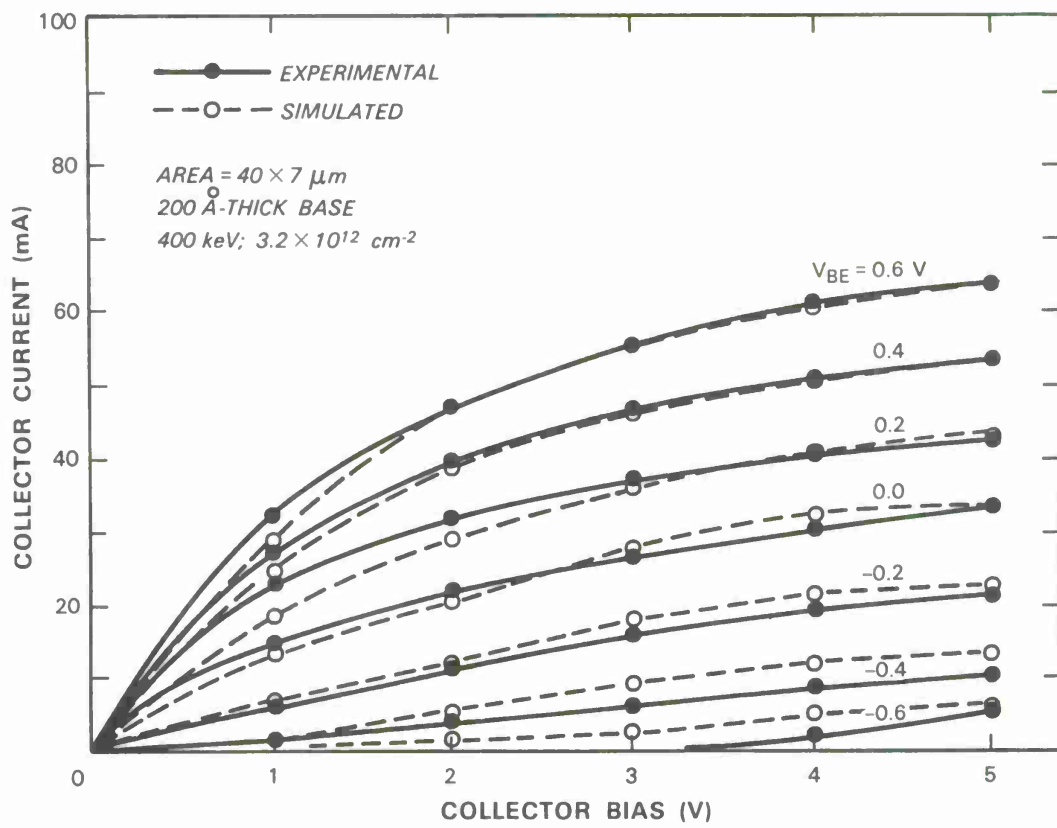


Figure 4-6. A comparison of experimental collector I-V characteristics and those obtained by CANDE for a 400-keV implanted device.

80537-26

4.3 A NEW METHOD FOR FINDING THE ENERGY SPECTRA OF QUANTUM-WELL STRUCTURES

QW structures now have been used in a number of different devices, including resonant tunneling diodes for millimeter-wave applications,⁴ spatial light modulators,⁵ and photoionization detectors⁶ for the IR region. Prior to the growth and fabrication of these devices, it is desirable to predict accurately the resonant tunneling transmission spectra or bound state energies as a function of applied electric field. The simplest way to find these spectra is first to discretize the spatially varying electron potential energy into a sequence of uniform-potential regions having width dictated by the required accuracy of the solutions. From this point, the standard approach has been to apply the so-called transfer-matrix method, in which the analytic wavefunction in each uniform potential region is related to the wavefunction in adjacent regions by a 2×2 matrix whose components are determined by the connection equations at each boundary. While providing accurate solutions to the majority of problems, the transfer-matrix method displays a few shortcomings mentioned below.

An alternative approach follows from the similarity of the problem at hand to that of standing electromagnetic waves on a set of uniform transmission lines in series. In the quantum problem, both the wave function Ψ and the derivative $\hbar m^{-1}d\Psi/dx$, are continuous across any point in space. Thus their ratio, a quantity we call the quantum impedance, is itself continuous, and in a region of uniform potential energy can be written

$$Z(x) = \frac{\Psi}{\hbar m^{-1}d\Psi/dx} = \frac{A\exp(\Gamma x) + B\exp(-\Gamma x)}{\hbar\Gamma m^{-1}[A\exp(\Gamma x) - B\exp(-\Gamma x)]} \quad (4-1)$$

where m is the effective mass, and Γ , the quantum propagation constant, is related to the kinetic energy through the relation $\Gamma = [(2m(V - E))^{1/2}/\hbar]$. Manipulation of Equation (4-1) then leads to the following relation between the impedance at two points, x and y

$$Z(y) = Z_C \left[\frac{Z(x) + Z_C \tanh[\Gamma(y - x)]}{Z_C + Z(x) \tanh[\Gamma(y - x)]} \right] \quad (4-2)$$

where $Z_C = (\hbar\Gamma/m)^{-1}$ is the characteristic quantum impedance. Thus if the characteristic impedance is known at any point in space, it can be found in all other regions using Equation (4-2) and the fact that $Z(y)$ is continuous across any step discontinuity in the potential energy.

This method is applied first to the resonant-tunneling problem. Resonant tunneling is a process for which the electron transmission probability through a QW structure displays at least one sharp peak as a function of the longitudinal kinetic energy of the incident electron. On the side of incidence, the electron wavefunction is expressed as the sum of incident and reflected components given by the numerator in Equation (4-1). On the opposite side, only a transmitted component is present, so that in the uniform potential approximation, the wavefunction has either $\exp(\Gamma x)$ or $\exp(-\Gamma x)$ behavior. Consequently, the quantum impedance at all points in this region is, within a sign, $Z(x) = Z_T = (\hbar\Gamma/m)^{-1}$. Working backwards through the structure, we use Equation (4-2) to relate the impedance at the first boundary between uniform-potential regions to Z_T , the impedance at the second boundary to that calculated at the first, and so on, until the impedance Z_I at the boundary formed with the incident side is obtained. The reflection coefficient through the structure is given by

$$R = \left[\frac{Z_I - Z_0}{Z_I + Z_0} \right]^2 \quad (4-3)$$

where Z_0 is the characteristic impedance in the incident region. The transmission coefficient is then found from $T = 1 - R$.

Shown in Figure 4-7 is a resonant-tunneling structure for which the impedance method is well suited, but for which the transfer-matrix method fails as explained below. It is also a structure that currently is being studied experimentally as a means to detect ballistic electrons in GaAs. It consists of two pairs of GaAs/AlAs double-barrier structures separated by a 500-Å-long region of undoped GaAs. Shown in Figure 4-8 is the theoretical transmission coefficient with a total voltage drop of 0.7 V across the structure.

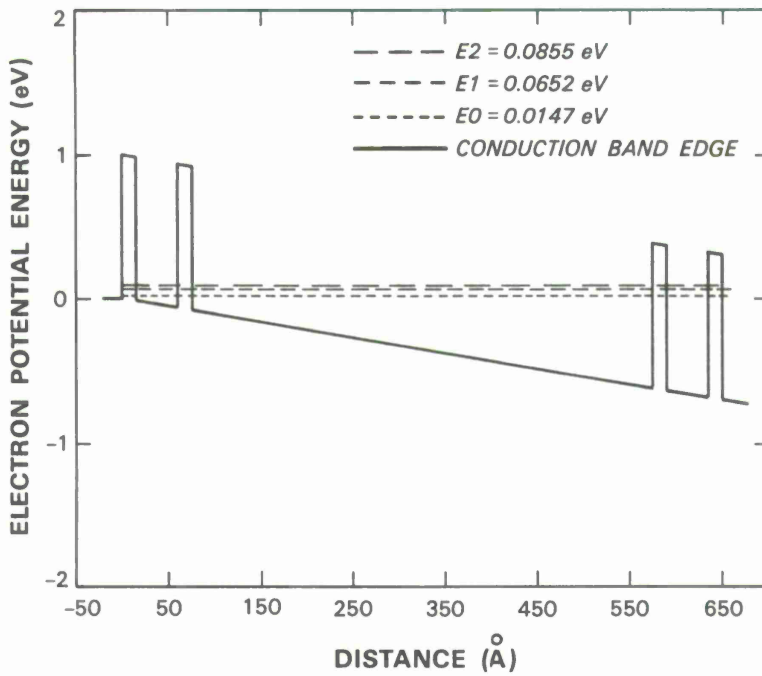


Figure 4-7. Electron potential energy diagram of a resonant-tunneling heterostructure with 0.7-V bias applied. Structure consists of a pair of double-barrier structures separated by 500 Å undoped GaAs. Each double-barrier structure has two 15-Å-wide AlAs regions separated by a 45-Å-wide GaAs QW. Three dashed energy levels (drawn to scale) correspond to three peaks in transmission probability curve shown in Figure 4-8.

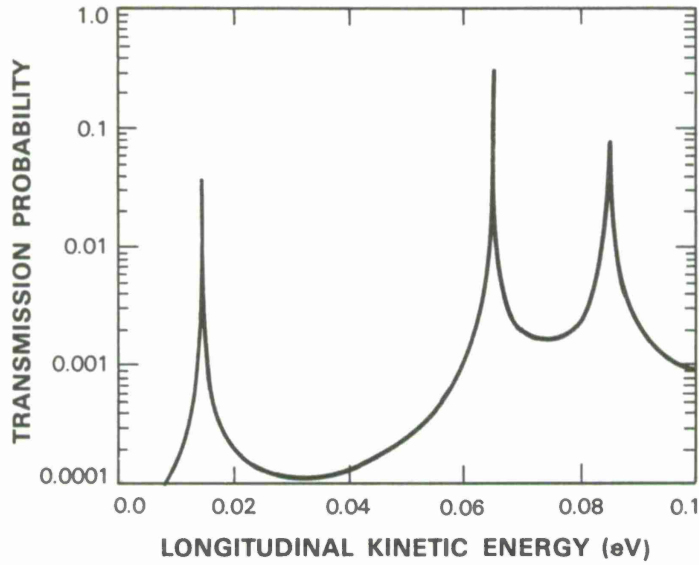


Figure 4-8. Transmission probability vs longitudinal kinetic energy for an electron incident on structure shown in Figure 4-7. A voltage drop of 0.7 V is assumed to exist across structure.

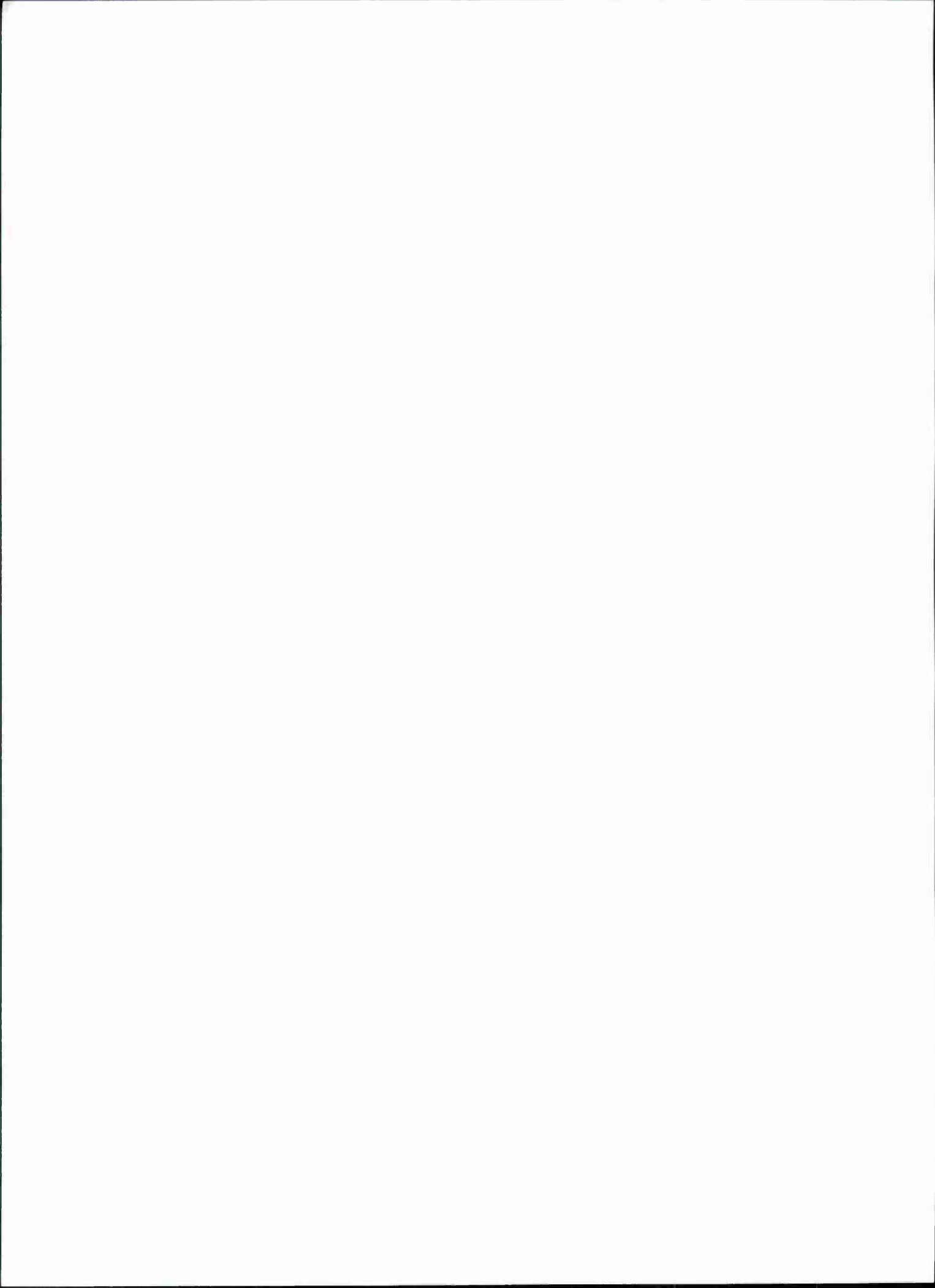
In problems involving isolated QWs having bound states, the impedance method is applied by noting that in both the left and right forbidden regions, the wavefunctions are decaying exponentials. Thus for any electron energy, the characteristic impedance in these two regions is immediately known: $Z_L = (\hbar\Gamma_L/m_L)^{-1}$ and $Z_R = (\hbar\Gamma_R/m_R)^{-1}$. The bound-state energies will be those for which the characteristic impedance on one side is transformed to a value exactly equal to the characteristic impedance on the opposite side after the recursive application of Equation (4-2) through all uniform-potential regions of the structure.

In both the stationary-state and resonant-tunneling problems, the quantum-impedance method is superior to the transfer-matrix method in at least two respects. First, it performs far fewer multiplications than the transfer-matrix method and, therefore, runs about twice as fast in most instances. Second, the impedance method is much less prone to the floating-point underflow and overflow errors incurred by the transfer-matrix method in relatively large structures.

E.R. Brown
K. Anderson

REFERENCES

1. Solid State Research Report, Lincoln Laboratory, MIT (1985:4), p. 37, DTIC AD-A172872.
2. I. Deyhimy, R.C. Eden, and J.S. Harris, IEEE Trans. Electron Devices, **ED-27**, 1127 (1980).
3. Technology Modeling Associates, Palo Alto, California.
4. T.C.L.G. Sollner, E.R. Brown, and W.D. Goodhue, Microwave and Millimeter-Wave Resonant Tunneling Diodes, Picosecond Electronics and Optoelectronics Technical Digest **87-1** (Optical Society of America, Washington, D.C. 1987), pp. 143-145
5. W.D. Goodhue, B.E. Burke, K.B. Nichols, G.M. Metze, and G.D. Johnson, J. Vac. Sci. Technol. B **4**, 769 (1986).
6. F. Capasso, K. Mohammed, and A.Y. Cho, IEEE J. Quantum Electron. **QE-22**, 1853 (1986).
7. A. Harwit, J.S. Harris, Jr., and A. Kapitulnik, J. Appl. Phys. **60**, 3211 (1986).



5. ANALOG DEVICE TECHNOLOGY

5.1 HIGH-TRANSITION-TEMPERATURE OXIDE SUPERCONDUCTORS

The new high-transition-temperature (high- T_c) oxide superconductors¹ hold substantial promise for many applications, including superconductive electronics. We have initiated a program to harness these new superconductors in the analog signal-processing devices presently being implemented in our Nb-based technology.² Key issues that will be addressed at the outset include the current-carrying capability of the high- T_c superconductors and the conductor loss at gigahertz (and higher) frequencies.

As a first step, we have successfully prepared bulk samples of the high- T_c compounds $\text{La}_{1.85}\text{Sr}_{0.15}\text{CuO}_4$ and $\text{YBa}_2\text{Cu}_3\text{O}_7$ using ceramic-processing techniques.³ Bulk samples are useful to investigate because of their relative ease of synthesis, which allows for greater flexibility in varying crucial processing parameters. Optimized materials then can provide information on the current-carrying capability of the superconductor, especially its relationship to the microstructure.

The transition temperature of an $\text{La}_{1.85}\text{Sr}_{0.15}\text{CuO}_4$ sample is shown in Figure 5-1. The mid-point of the transition is 38 K, and the transition width (10- to 90-percent full transition) is 5 K.

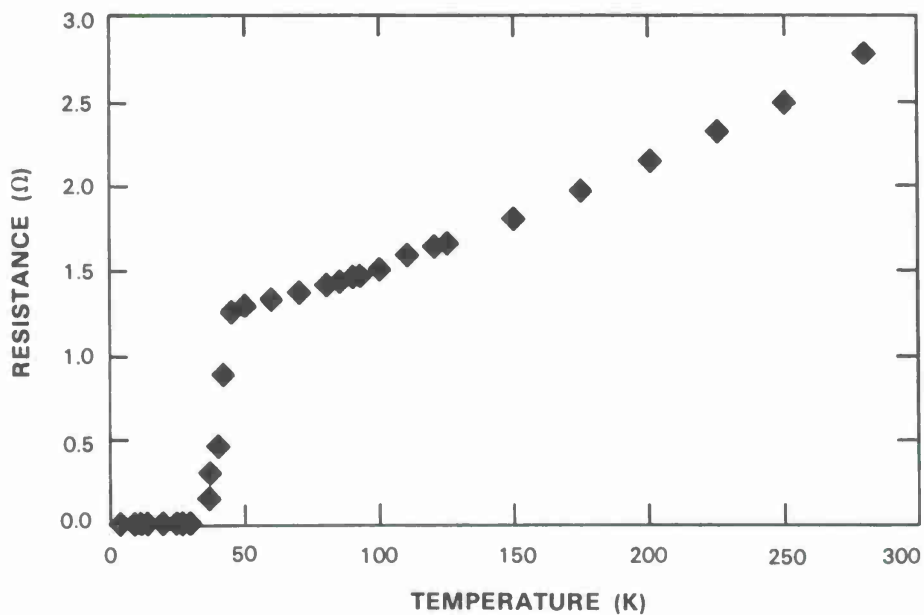


Figure 5-1. *Dc resistance as a function of temperature for bulk $\text{La}_{1.85}\text{Sr}_{0.15}\text{CuO}_4$.*

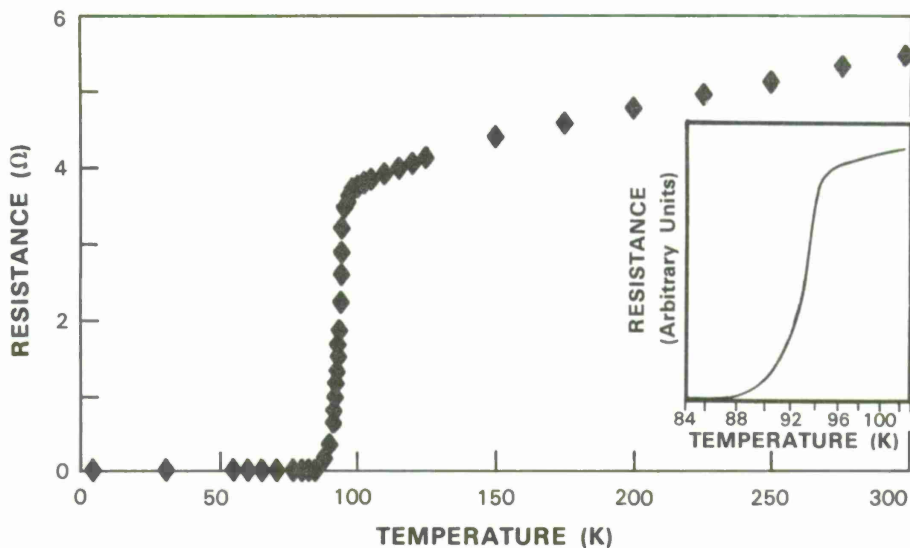


Figure 5-2. *Dc resistance as a function of temperature for bulk $YBa_2Cu_3O_7$.*

The transition temperature for a $YBa_2Cu_3O_7$ sample is shown in Figure 5-2. The inset shows an expanded view of the transition region. (The temperature scale is slightly nonlinear since it is proportional to the resistance of the Ge thermometer.) The midpoint of the transition is 93 K and the transition width (10- to 90-percent full transition) is 3 K. X-ray analysis confirmed that this sample consists mostly of the desired high- T_c orthorhombic crystal phase. Subsequent processing improvements have led to entirely single-phase samples.

Efforts are currently underway to prepare superconducting thin films by both e-beam evaporation and RF magnetron sputtering. Initial measurements on films deposited by e-beam evaporation show an onset of superconductivity at 95 K. Both thin-film and bulk materials are being tailored for use in a stripline resonator measurement⁴ which will provide a direct measurement of the conductor losses at higher frequencies, from which can be inferred the superconducting energy gap.

M.S. DiIorio E.J. Delaney
 A.J. Strauss B-Y. Tsaur

5.2 INTEGRATED CIRCUIT IMPLEMENTATION OF AN ARTIFICIAL NEURAL NETWORK BASED ON CCD AND MNOS TECHNOLOGIES

A Si integrated circuit which implements a dense array of synaptic coupling elements for an artificial neural network has been designed and fabricated⁵ using charge-coupled device (CCD) and metal-nitride-oxide-semiconductor (MNOS) technologies.⁶⁻⁷ The coupling strengths of the elements are analog and nonvolatile, and they may be reprogrammed entirely under electrical control at any time during the operation of the device. The performance of this coupling matrix has been studied by operating it in a Hopfield iterative feedback network, as shown in Figure 5-3.

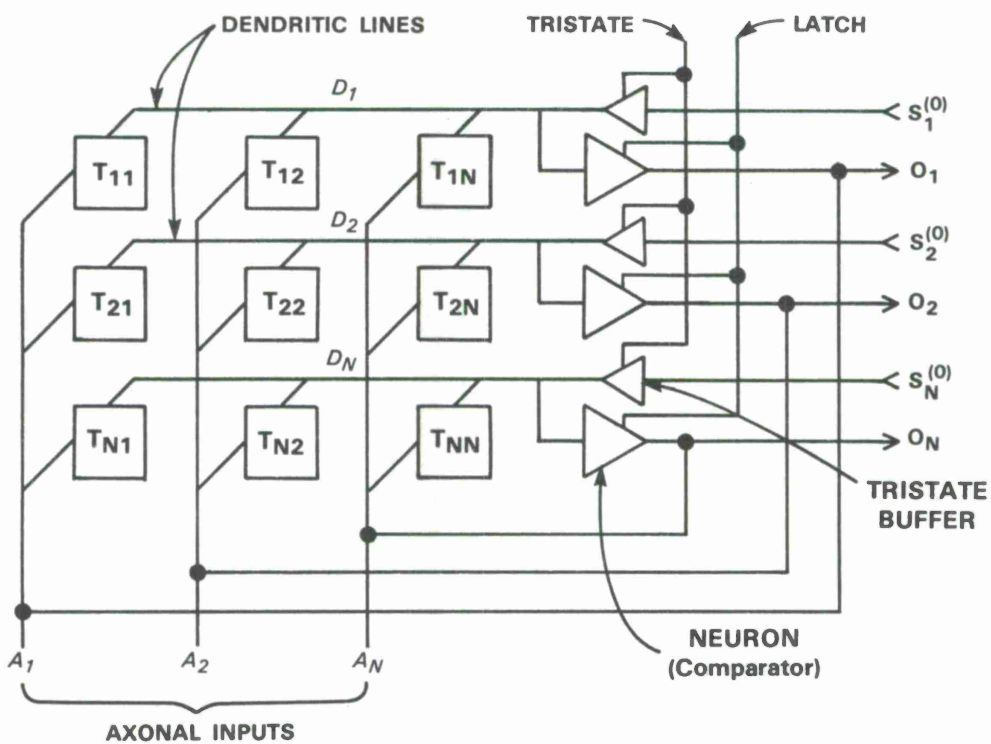


Figure 5-3. $N \times N$ Hopfield associative memory.

The chip contains the coupling elements and sense amplifiers, while off-chip peripheral circuits provide the nonlinear operations and feedback control.

For the Hopfield model,⁸⁻¹⁰ the synaptic weights are defined by a Hebbian or outer-product learning rule of the form

$$T = \sum_{x=1}^M |F^x\rangle \langle F^x| \text{ or } T_{ij} = \sum_{x=1}^M F^x_i F^x_j \quad (5-1)$$

where the M facts $|F^x\rangle$ stored by the network are each N -dimensional binary state vectors with component values of ± 1 .

The retrieval of the facts stored in the network is accomplished associatively by iteratively multiplying an input vector $|S\rangle$ by the matrix T and taking the sign of the components of the resulting vector. Specifically, if an input state $|S^0\rangle$ (where the superscript indicates the iteration number) is presented to the network, it evolves according to the following equation:

$$S_i^{(p+1)} = \text{sign} \sum_{j=1}^N T_{ij} S_j^{(p)} \quad (5-2)$$

When the network operates successfully, the system converges to a state which does not change upon iteration, and this stable state is the stored fact that most resembles $|S^{(0)}\rangle$.

As a requirement for the implementation of the Hopfield model, each synapse must be capable of both excitatory and inhibitory operation and each must be able to accommodate both positive and negative signals on the axons and dendrites. To accomplish this, and at the same time to make the circuit highly tolerant of processing variations across a chip, a fully differential design was implemented, as shown in Figure 5-4. Each neuron (comparator) has two input dendrites, one for positive signals (D_i) and one for negative or inhibitory signals (\bar{D}_i), and two axonal output lines, again one for positive signals (A_j) and one for negative signals (\bar{A}_j). Each synapse contains two MNOS elements (M_{ij} , \bar{M}_{ij}). The T_{ij} coupling strengths are represented by the difference between the flat-band voltages of these two MNOS elements; the vector-matrix product operation is performed using charge-coupling techniques. A state vector component of +1 is represented in the circuit by a signal on the normal line, and a -1 component is represented by a signal on the "bar" line.

The two dendrite lines D_i and \bar{D}_i are implemented as diffusions and act as sources and drains for the CCD structure. The memory structures M_{ij} and \bar{M}_{ij} are CCD storage wells whose gates have an MNOS nitride/tunnel-oxide dual dielectric. The structures labeled HW are CCD

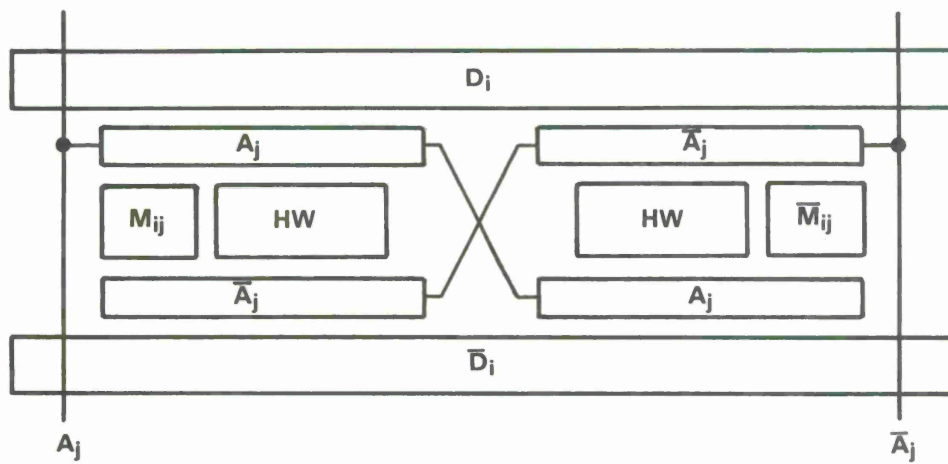


Figure 5-4. Single synaptic element showing fully balanced structure.

holding wells with conventional gates. Finally, the axon lines A_j and \bar{A}_j are CCD transfer gates that control the movement of charge between the storage wells and the source/drain diffusions. Note that there are four axonal gates that are cross-connected.

The Hebbian or outer-product learning rule of Equation (5-1) requires that the flat-band voltage of the positive memory element M_{ij} be increased when either (1) both D_i and A_j are active ($+1 \cdot +1 = +1$), or (2) both \bar{D}_i and \bar{A}_j are active ($-1 \cdot -1 = +1$). If one bar line and one normal line are active, then the flat-band voltage of the negative memory element M_{ij} must be increased. The structure in Figure 5-4 accomplishes this in a single operation. Though we will not present the operating waveforms or describe the operations in detail, the principles can be understood. During a learning cycle, only one of the two dendritic lines is active and is pulsed to make a source of charge available. At that time, only one axonal line will be active and allow the charge to pass into the holding well. Since the positive holding well is connected on the top to normal dendrite and axon lines and on the bottom to barred dendrite and axon lines, the required charge transfer takes place. Similarly, the barred holding well on the right is connected to one normal and one barred line both above and below.

A retrieval cycle [Equation (5-2)] is also accomplished in a single operation. Initially, the axons are set to the input state $|S^0\rangle$ by activating the tristate latches and comparators. Thereafter, recall cycles begin with a pulse applied to both dendritic lines. Since each memory well is connected to dendrite diffusions by both a normal and a barred axon line, both memory wells will be filled with charge from one side or the other. After this has taken place, the dendritic lines are biased to a below-threshold reference level, and the bias on the memory wells is reduced to force the charge out. This charge will flow over the active axon gate. Thus, if line A_j is active, the charge in the positive (normal) memory well will flow onto the positive (normal) dendrite, and the charge in the negative (barred) memory well will flow onto the negative (barred) dendrite. The net signal recorded by the dendrites is the difference between the charges received on the two lines. Similarly, if the barred axon line \bar{A}_j is active, the two memory-well charges will flow onto the opposite dendrite lines, and the net signal contributed to the neuron will be the negative of what it was in the first case.

A photograph of the prototype integrated circuit is shown in Figure 5-5. The chip contains a 13×13 array of synaptic couplers, 26 summing diffusions (2 per row), and 26 output-buffer amplifiers and reset transistors (1 per diffusion). The buffer amplifiers are single-transistor source followers with off-chip loads. The fabrication of this device required three levels of polysilicon, an n^+ diffusion implant, and one level of metal to define the charge coupling gates and the interconnections. With $4\text{-}\mu\text{m}$ design rules, the size of each synaptic element is $90 \times 50 \mu\text{m}$.

We have performed two preliminary experiments with the chip, using only 9 of the 13 neurons. In the first experiment, we stored one state $|F^1\rangle$ in the memory and then exercised the memory by presenting all possible input states that differed from $|F^1\rangle$ in from 0 to 3 bit positions. The results, shown in the left half of Figure 5-6, conformed well to the results expected theoretically. For the next experiment, we applied a second state $|F^2\rangle$ and incrementally stored it in the MNOS devices in the synapses. We then presented all input states that differed from

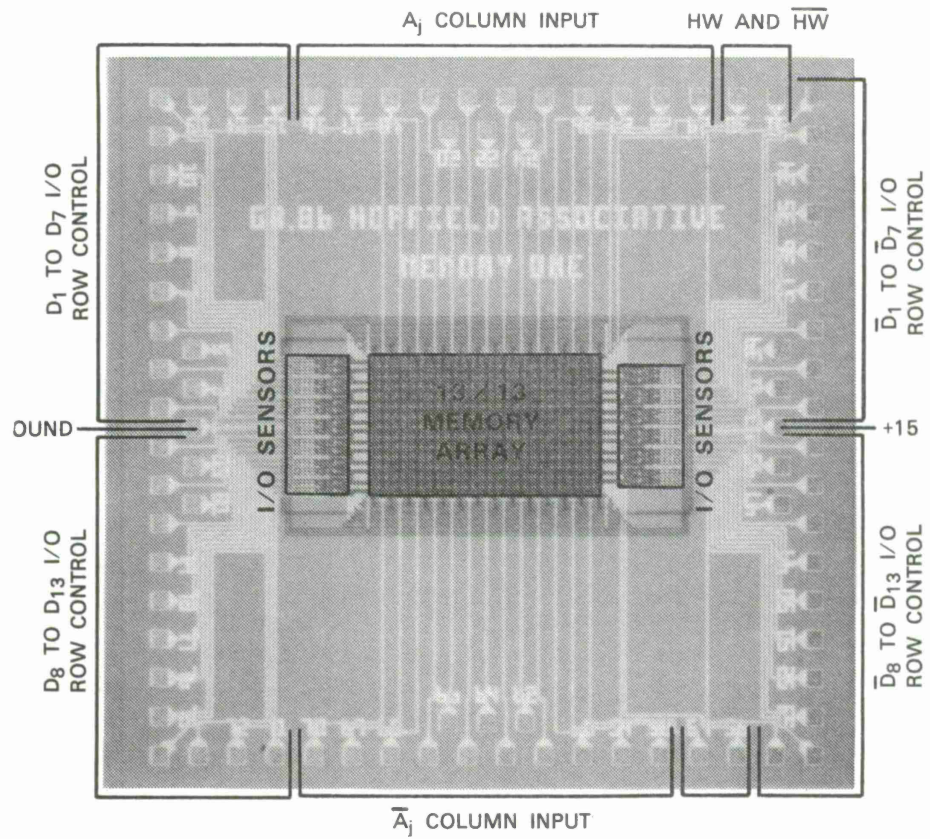


Figure 5-5. Prototype MNOS/CCD artificial neural-network integrated circuit.

80637-33

either of the two F states in from 0 to 3 bit positions. The results of that experiment are shown in the right half of Figure 5-6.

To summarize, we have designed, fabricated, and tested an artificial neural-network integrated circuit that can be erased, programmed and reprogrammed electrically, and which retains its memory without application of power. We demonstrated not only that the chip could be programmed, but also that additional information could be accumulated in the chip incrementally.

K.E. Thompson
J.P. Sage

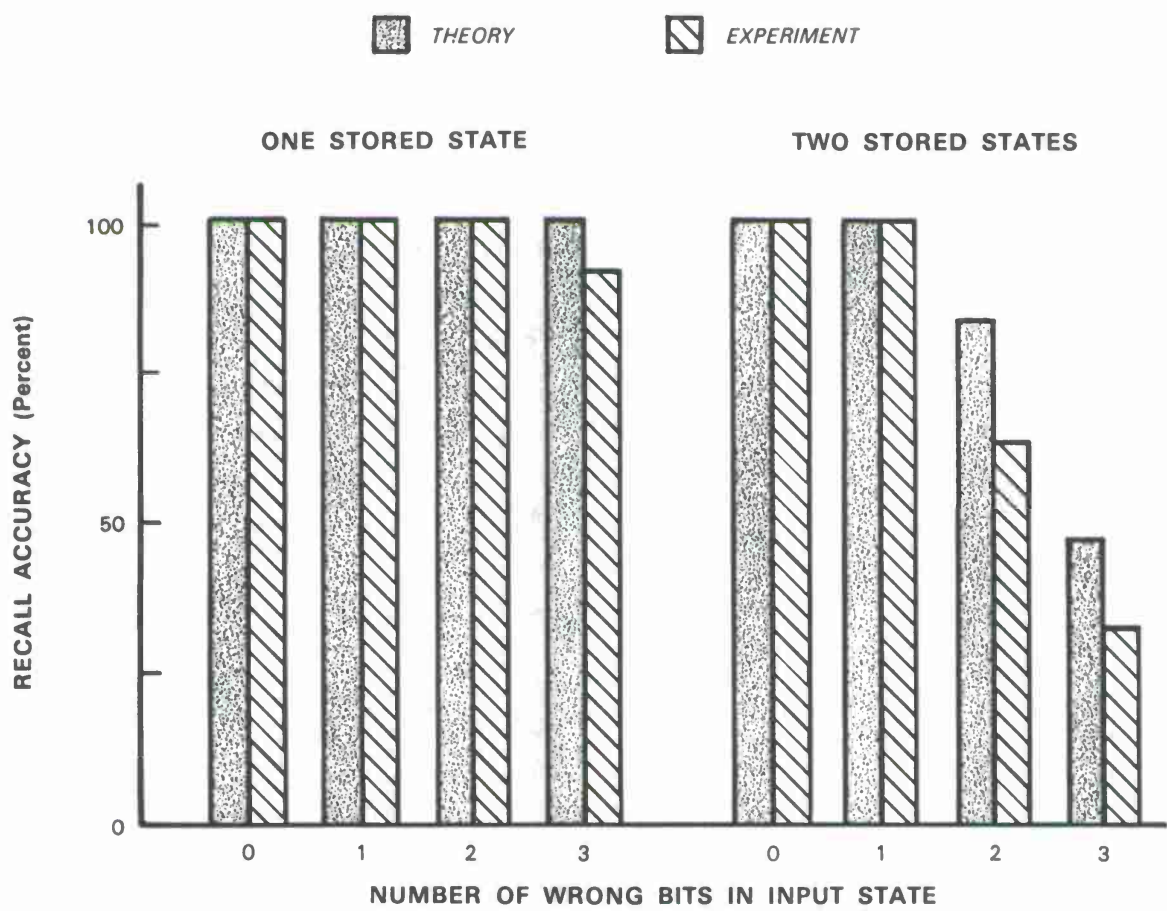


Figure 5-6. Experimental vs theoretical associative-recall performance of artificial neural network.

REFERENCES

1. Physics Today **40**, 17 (1987).
2. R.S. Withers, A.C. Anderson, J.B. Green, and S.A. Reible, IEEE Trans. Magn. **MAG-21**, 186 (1985).
3. See, for example, R.J. Cava, R.B. VanDover, B. Batlogg, and E.A. Rietman, Phys. Rev. Lett. **58**, 408 (1987).
4. A.C. Anderson, R.S. Withers, S.A. Reible, and R.W. Ralston, IEEE Trans. Magn. **MAG-19**, 485 (1983).
5. K.E. Thompson, S.M. Thesis, MIT Department of Electrical Engineering and Computer Science, 1987.
6. R.S. Withers, R.W. Ralston, and E. Stern, IEEE Electron Device Lett. **EDL-1**, 42 (1980), DDC AD-A096617/6.
7. R.S. Withers, D.J. Silversmith, and R.W. Mountain, IEEE Electron Device Lett. **EDL-2**, 165 (1981), DTIC AD-A107229/7.
8. J.J. Hopfield, Proc. Natl. Acad. Sci. USA **79**, 2554 (1982).
9. J.J. Hopfield, D.I. Feinstein, and R.G. Palmer, Nature **304**, 158 (1983).
10. J.J. Hopfield, Proc. Natl. Acad. Sci. USA **81**, 3088 (1984).

UNCLASSIFIED

SECURITY CLASSIFICATION OF THIS PAGE

REPORT DOCUMENTATION PAGE

1a. REPORT SECURITY CLASSIFICATION Unclassified		1b. RESTRICTIVE MARKINGS	
2a. SECURITY CLASSIFICATION AUTHORITY		3. DISTRIBUTION/AVAILABILITY OF REPORT Approved for public release; distribution unlimited.	
2b. DECLASSIFICATION/DOWNGRADING SCHEDULE			
4. PERFORMING ORGANIZATION REPORT NUMBER(S) 1987:2		5. MONITORING ORGANIZATION REPORT NUMBER(S) ESD-TR-87-040	
6a. NAME OF PERFORMING ORGANIZATION Lincoln Laboratory, MIT	6b. OFFICE SYMBOL (If applicable)	7a. NAME OF MONITORING ORGANIZATION Electronic Systems Division	
6c. ADDRESS (City, State, and Zip Code) P.O. Box 73 Lexington, MA 02173-0073		7b. ADDRESS (City, State, and Zip Code) Hanscom AFB, MA 01731	
8a. NAME OF FUNDING/SPONSORING ORGANIZATION Air Force Systems Command, USAF	8b. OFFICE SYMBOL (If applicable)	9. PROCUREMENT INSTRUMENT IDENTIFICATION NUMBER F19628-85-C-0002	
8c. ADDRESS (City, State, and Zip Code) Andrews AFB Washington, DC 20334		10. SOURCE OF FUNDING NUMBERS PROGRAM ELEMENT NO. 63250F PROJECT NO. 649L TASK NO. WORK UNIT ACCESSION NO.	
11. TITLE (Include Security Classification) Solid State Research			
12. PERSONAL AUTHOR(S) Alan L. McWhorter			
13a. TYPE OF REPORT Quarterly Technical Report	13b. TIME COVERED FROM 1 Feb TO 30 Apr 87	14. DATE OF REPORT (Year, Month, Day) 1987, May 15	15. PAGE COUNT 76
16. SUPPLEMENTARY NOTATION None			
17. COSATI CODES		18. SUBJECT TERMS (Continue on reverse if necessary and identify by block number)	
FIELD	GROUP	SUB-GROUP	solid state devices quantum electronics materials research microelectronics analog device technology ion implantation optical modulators lasers quantum-well effects nonlinear optics charge-coupled devices microwave semiconductor devices superconductors neural networks
19. ABSTRACT (Continue on reverse if necessary and identify by block number)			
This report covers in detail the solid state research work of the Solid State Division at Lincoln Laboratory for the period 1 February through 30 April 1987. The topics covered are Solid State Device Research, Quantum Electronics, Materials Research, Microelectronics, and Analog Device Technology. Funding is provided primarily by the Air Force, with additional support provided by the Army, DARPA, Navy, SDIO, NASA, and DOE.			
20. DISTRIBUTION/AVAILABILITY OF ABSTRACT <input type="checkbox"/> UNCLASSIFIED/UNLIMITED <input checked="" type="checkbox"/> SAME AS RPT. <input type="checkbox"/> DTIC USERS		21. ABSTRACT SECURITY CLASSIFICATION Unclassified	
22a. NAME OF RESPONSIBLE INDIVIDUAL Maj. Thomas J. Alpert, USAF		22b. TELEPHONE (Include Area Code) (617) 863-5500, X-2330	22c. OFFICE SYMBOL ESD/TML

